Three-dimensional anisotropic pressure free boundary equilibria

W. A. Cooper[a,1], S. P. Hirshman[b], P. Merkel[c], J. P. Graves[a], J. Kisslinger[c],

H. F. G. Wobig[c], Y. Narushima[d], S. Okamura[d] and K. Y. Watanabe[d]

[a] *Ecole Polytechnique Fédérale de Lausanne, Centre de Recherches en Physique des Plasmas, Association Euratom-Suisse, CH1015 Lausanne, Switzerland*

[b] *Fusion Energy Division, Oak Ridge National Laboratory, Oak Ridge, TN, USA*

[c] *Max Planck Institut für Plasmaphysik, Garching, Germany*

[d] *National Institute for Fusion Science, Oroshi-cho 322-6, Toki-shi 509-5292, Japan*

Free boundary three-dimensional anisotropic pressure magnetohydrodynamic equilibria with nested magnetic flux surfaces are computed through the minimisation of the plasma energy functional $W = \int_V d^3x d^3x \left[B^2/(2\mu_0) + p_{||}/(\Gamma - 1)\right]$. The plasma-vacuum interface is varied to guarantee the continuity of the total pressure $[p_\perp + B^2/(2\mu_0)]$ across it and the vacuum magnetic field must satisfy the Neumann boundary condition that its component normal to this interface surface vanishes. The vacuum magnetic field corresponds to that driven by the plasma current and external coils plus the gradient of a potential function whose solution is obtained using a Green's function method. The energetic particle contributions to the pressure are evaluated analytically from the moments of the variant of a bi-Maxwellian distribution function that satisfies the constraint $\mathbf{B} \cdot \nabla \mathcal{F}_h = 0$. Applications to demonstrate the versatility and reliability of the numerical method employed have concentrated on high-β off-axis energetic particle deposition with

[1]W. A. Cooper, Centre de Recherches en Physique des Plasmas, Ecole Polytechnique Fédérale de Lausanne, Station 13, 1015 Lausanne, Switzerland.

Tel: +41216933452,

e-mail: wilfred.cooper@epfl.ch

large parallel and perpendicular pressure anisotropies in a 2-field period quasiaxisymmetric stellarator reactor system. For large perpendicular pressure anisotropy, the hot particle component of the $p_\perp$ distribution localises in the regions where the energetic particles are deposited. For large parallel pressure anisotropy, the pressures are more uniform around the flux surfaces.

PACS: $52.55.Hc; 52.65.Kj$

Keywords: free boundary equilibrium, Bi-Maxwellian, pressure anisotropy, Green's function, quasiaxisymmetry.

1. Introduction

Auxiliary heating methods are required in magnetic confinement devices to achieve the high temperatures necessary for thermonuclear conditions. The schemes employed, however, tend to generate populations of energetic particles that are nonuniformly distributed in velocity space. The Large Helical Device (LHD) heliotron has a $14MW$ tangential neutral beam injection system based on negative ion beam technology that delivers $180keV$ fast ions that produce a large parallel pressure anisotropy inasmuch as the ratio parallel to perpendicular stored energies have been measured in the range of $3-4$ [1]. Furthermore, the hot ions make a substantial contribution to the volume averaged β that can exceed $1/3$ of the total value [2]. In the JET tokamak experiment, radio frequency waves in the ion cyclotron range can produce a significant perpendicular pressure anisotropy that can be very accurately described with a bi-Maxwellian distribution function for the energetic ions [3] which can contribute $1/4$ of the total estimated volume averaged β.

The three-dimensional (3D) magnetohydrodynamic equilibrium code VMEC [4] coupled with the NESTOR vacuum solver [5] computes general toroidal free boundary scalar pressure equilibria with nested magnetic flux surfaces [6]. The goal of this work is to extend this code to anisotropic pressure conditions driven by the energetic particle species. We have labelled this code extension with the acronym ANIMEC (Anisotropic Neumann Inverse Moments Equilibrium Code). The hot particles are modelled with the variant of a bi-Maxwellian distribution function which satisfies the constraint imposed by the leading order solution of the Fokker-Planck equation that $\mathbf{B} \cdot \nabla \mathcal{F}_h = 0$. This model is very convenient because the pressure moments of the distribution function can be determined analytically and it allows for the deposition of hot particles in any region of the plasma. It is particularly useful to describe hot populations generated with ion cyclotron resonance heating (ICRH) [7, 8] and has been previously implemented and applied with success in a fixed boundary version of the 3D VMEC code [9].

Anisotropic pressure equilibrium solvers have been previously developed for axisymmetric [10, 11, 12] and helically symmetric [13, 14] geometries. For 3D stellarator configurations, an expansion method was applied in which the pressures are imposed to be only a function of the radial variable [15]. More recently, fixed boundary equilibria based on the VMEC code have been devised, in addition to the bi-Maxwellian model [9], using slowing down distribution functions multiplied by a factor $(\mu B_{min}/\mathcal{E})^{\ell}$ to obtain large perpendicular anisotropy concentrated on the low field (LF) side [16] and by a factor $(1-\mu B_{min}/\mathcal{E})^{\ell}$ to obtain large parallel anisotropy [17]. Here, B_{min} is the minimum value of the magnetic field strength B on each flux surface, ℓ is an integer that controls the level of anisotropy while μ and $\mathcal{E}$ represent the particle magnetic moment and energy, respectively. These distribution functions have the disadvantage, unlike the bi-Maxwellian, of becoming singular at the velocity space coordinate origin, though their pressure moments remain finite and therefore adequate for equilibrium calculations.

The bi-Maxwellian distribution function model we have invoked, the parallel and perpendicular pressures that can be derived from it and other useful equilibrium relations are outlined in Section 2. The magnetohydrodynamic equilibrium energy valid for anisotropic pressure plasmas is presented in Section 3 which also includes details of the minimisation method. The vacuum treatment using a Green's function approach is briefly described in Section 4. The radial force balance diagnostic that determines the precision of the numerical equilibrium state obtained is considered in Section 5. Applications of ANIMEC to a 2-field period quasiaxisymmetric stellarator reactor is addressed in Section 6 while the summary and conclusions are discussed in Section 7.

2. The bi-Maxwellian distribution function and its pressure moments [8]

We consider a variant of the standard bi-Maxwellian distribution function to describe the hot particles which satisfies the condition imposed by the lowest order solution of the Fokker-Planck equation, namely, $\mathbf{B} \cdot \nabla \mathcal{F}_h = 0$, which can be expressed as

$$\mathcal{F}_h(s, \mathcal{E}, \mu) = \mathcal{N}(s)\Big(\frac{m_h}{2\pi T_\perp(s)}\Big)^{3/2} \exp\Big[-m_h\Big(\frac{\mu B_c}{T_\perp(s)} + \frac{|\mathcal{E} - \mu B_C|}{T_{||}(s)}\Big)\Big]. \tag{1}$$

where $\mathcal{F}_h$ is the fast particle distribution, $\mathcal{N}$ is the label of the density-like amplitude factor, m_h, $T_\perp$ and $T_{||}$ represent the energetic particle mass, perpendicular temperature and parallel temperature, respectively, s is a radial variable proportional to the toroidal magnetic flux $2\pi\Phi$ enclosed and B_C corresponds to a critical magnetic field that identifies the layer where the energetic particles are deposited. In principle, B_C can depend on the flux surface variable s, but for simplicity we have chosen it to be a constant. This model distribution function with constant B_C fits fast particle distributions computed with Fokker-Planck solvers that describe solutions with ICRH particularly well. The contours of constant distribution of particles in $v_\perp$ versus $v_{||}$ space is displayed in Fig. 1 for an example where the hot particle temperature ratio $T_\perp/T_{||} = 4.2$ at a position for which $B_C/B = 1.3$. The example shown is not a pure bi-Maxwellian but contains also a thermalised Maxwellian component that is 10% of the total distribution for which the thermal temperature is 5% of $T_\perp$. This makes the shape of the contours close to the origin to be more uniform and realistic in $v_\perp$ versus $v_{||}$ space.

The hot particle parallel pressure moment of the bi-Maxwellian distribution function shown in Eqn. (1) can be integrated analytically to yield

$$p^h_{||}(s, B) = \mathcal{N}(s) T_{||}(s) H(s, B), \tag{2}$$

where the scale factor $H(s, B)$ governs that variation of the pressures around a magnetic

flux surface and, for $B > B_C$, is given by

$$H(s,B) = \frac{(B/B_C)}{\left[1 - \frac{T_\perp}{T_\parallel}\left(1 - \frac{B}{B_C}\right)\right]}, \tag{3}$$

while for $B < B_C$ one obtains

$$H(s,B) = \frac{B}{B_C}\frac{\left[1 + \frac{T_\perp}{T_\parallel}\left(1 - \frac{B}{B_C}\right) - 2\left(\frac{T_\perp}{T_\parallel}\right)^{5/2}\left(1 - \frac{B}{B_C}\right)^{5/2}\right]}{\left[1 - \left(\frac{T_\perp}{T_\parallel}\right)\left(1 - \frac{B}{B_C}\right)\right]\left[1 + \left(\frac{T_\perp}{T_\parallel}\right)\left(1 - \frac{B}{B_C}\right)\right]}. \tag{4}$$

The total parallel pressure is $p_{||}(s,B) = p(s) + p^h_{||}(s,B)$, where $p(s)$ corresponds to the contribution of the thermal species (plus the thermalised hot particles) in the plasma. Rather than determine the perpendicular pressure from the corresponding moment of the distribution function, we invoke the magnetodydrodynamic force balance parallel to the equilibrium magnetic field lines [9] to obtain

$$p_\perp(s,B) = p_\parallel(s,B) - B\frac{\partial p_\parallel}{\partial B}\bigg|_s. \tag{5}$$

Two criteria that must be monitored in an anisotropic pressure equilibrium calculation are the firehose stability relation [18]

$$\sigma \equiv \frac{1}{\mu_0} - \frac{1}{B}\frac{\partial p_\parallel}{\partial B}\bigg|_s = \frac{1}{\mu_0} - \frac{p_\parallel - p_\perp}{B^2} > 0 \tag{6}$$

and the mirror stability relation [18]

$$\tau \equiv \frac{\partial(\sigma B)}{\partial B}\bigg|_s = \frac{1}{\mu_0} + \frac{1}{B}\frac{\partial p_\perp}{\partial B}\bigg|_s > 0. \tag{7}$$

where $\mu_0 = 4\pi \times 10^{-7} H/m$ is the permeability of free space.

3. Equilibrium energy minimisation

The first variation of the energy functional

$$W = \int_V d^3x \Big(\frac{B^2}{2\mu_0} + \frac{p_\parallel(s,B)}{\Gamma - 1}\Big), \tag{8}$$

can be demonstrated to recover the magnetohydrodynamic force balance relation in magnetically confined plasmas with pressure anisotropy. The total parallel pressure is expressed in the form

$$p_{\|}(s,B) = M(s)[\Phi'(s)]^{\Gamma}\frac{1+p_h(s)H(s,B)}{\langle 1+p_h(s)H(s,B)\rangle^{\Gamma}}, \tag{9}$$

where $M(s)$ is the plasma mass enclosed within the surface labelled by s, $p_h(s)$ is the hot particle pressure scale factor, $H(s,B)$ has been defined in the previous section and the flux surface average of a function A is defined as

$$\langle A\rangle = \frac{L}{(2\pi)^2}\int_0^{2\pi/L} dv \int_0^{2\pi} du\sqrt{g}A(s,u,v). \tag{10}$$

The variables u and v of the inverse coordinate system (s,u,v) represent the poloidal and toroidal angular variables, respectively, that are used in the ANIMEC code [19]. The number of equilibrium field periods is denoted by L and $\sqrt{g}$ is the Jacobian of the transformation from the Cartesian frame to the (s,u,v) coordinates. The thermal pressure component in Eqn. (9) corresponds to $p(s) = M(s)[\Phi'(s)]^{\Gamma}/\langle 1+p_h(s)H(s,B)\rangle^{\Gamma}$, while the hot particle parallel pressure is $p_{||}^h = p(s)p_h(s)H(s,B)$. The identification $\mathcal{N}(s)T_{||}(s) = p(s)p_h(s)$ reconciles the description of the parallel pressure moment of the bi-Maxwellian distribution function [Eqn. (2)] with that given in Eqn. (9). For $\Gamma > 1$, the energy functional W is strictly positive-definite. However, for the applications we consider, we choose the adiabatic index $\Gamma = 0$.

A steepest descent energy minimisation procedure is applied to W in the inverse coordinate representation with respect to an artificial time parameter t to obtain

$$\begin{aligned}\frac{dW}{dt} = &- \int_V dsdudv\Big[F_R\frac{\partial R}{\partial t} + F_Z\frac{\partial Z}{\partial t} + F_\lambda\frac{\partial \lambda}{\partial t}\Big] \\ &- \int\int_{s=1} dudv\Big[R\Big(p_\perp + \frac{B^2}{2\mu_0}\Big)\Big(\frac{\partial R}{\partial u}\frac{\partial Z}{\partial t} - \frac{\partial Z}{\partial u}\frac{\partial R}{\partial t}\Big)\Big],\end{aligned} \tag{11}$$

where R is the distance from the major axis, Z is the distance from the vertical midplane and λ is the poloidal angle renormalisation parameter that controls the spectral width of the representation [19]. The forces within the plasma are

$$\begin{aligned}F_R = &\quad \frac{\partial}{\partial u}[\sigma\sqrt{g}B^u(\boldsymbol{B}\cdot\boldsymbol{\nabla}R)] + \frac{\partial}{\partial v}[\sigma\sqrt{g}B^v(\boldsymbol{B}\cdot\boldsymbol{\nabla}R)] \\ &- \frac{\partial}{\partial u}\Big[R\frac{\partial Z}{\partial s}\Big(p_\perp + \frac{B^2}{2\mu_0}\Big)\Big] + \frac{\partial}{\partial s}\Big[R\frac{\partial Z}{\partial u}\Big(p_\perp + \frac{B^2}{2\mu_0}\Big)\Big]\end{aligned} \tag{12}$$

$$
\begin{aligned}
&+ \quad \frac{\sqrt{g}}{R}\Big[\Big(p_\perp + \frac{B^2}{2\mu_0}\Big) - \sigma R^2 (B^v)^2\Big], \\
F_z = &\quad \frac{\partial}{\partial u}[\sigma\sqrt{g}B^u(\boldsymbol{B}\cdot\boldsymbol{\nabla}Z)] + \frac{\partial}{\partial v}[\sigma\sqrt{g}B^v(\boldsymbol{B}\cdot\boldsymbol{\nabla}Z)] \\
&+ \quad \frac{\partial}{\partial u}\Big[R\frac{\partial R}{\partial s}\Big(p_\perp + \frac{B^2}{2\mu_0}\Big)\Big] - \frac{\partial}{\partial s}\Big[R\frac{\partial R}{\partial u}\Big(p_\perp + \frac{B^2}{2\mu_0}\Big)\Big]
\end{aligned} \tag{13}
$$

and

$$
F_\lambda = \Phi'(s)\Big[\frac{\partial(\sigma B_v)}{\partial u} - \frac{\partial(\sigma B_u)}{\partial v}\Big]. \tag{14}
$$

Note that at the plasma-vacuum interface, the contributions to the horizontal force F_R and to the vertical force F_Z are $-R\left[p_\perp + B^2/(2\mu_0)\right]\partial Z/\partial u$ and $R\left[p_\perp + B^2/(2\mu_0)\right]\partial R/\partial u$, respectively.

The forces of the scalar pressure model are recovered by taking $\sigma \to 1/\mu_0$ and $p_\perp \to p$ [19]. The vanishing of Eqn. (14) reflects the condition that the current density lines $\mathbf{K} = \nabla\times(\sigma\mathbf{B})$ lie on the magnetic flux surfaces, namely $\mathbf{K}\cdot\nabla s = 0$. Equilibrium conditions are achieved when F_R, F_Z and F_λ approach 0 simultaneously. It is clear from Eqn. (11) that the variation of W is negative-definite when equating $\dot{R} = F_R$, $\dot{Z} = F_Z$ and $\dot{\lambda} = F_\lambda$. Further details of the minimisation procedure are reported in Ref. [19] and of the radial discretisation in Ref. [20]. When the forces described in Eqns. (12)-(14) achieve a prespecified level, a matrix preconditioning algorithm, GMRES [21], is called that can reduce the force level error substantially.

4. Green's function vacuum [5]

The magnetic field in the vacuum is represented as $\mathbf{B_V} = \mathbf{B_0} + \nabla\Phi_V$, where $\mathbf{B_0}$ corresponds to the field generated by the external coils and the plasma current in the vacuum domain and the potential Φ_V must satify the Neumann condition

$$
(\boldsymbol{B_0} + \boldsymbol{\nabla}\Phi_V)\cdot\boldsymbol{n_p} = 0 \tag{15}
$$

at the plasma-vacuum interface surface. In the region exterior to the plasma, the potential Φ_V also satisfies the Laplace equation $\Delta\Phi_V = 0$ and the condition at the plasma boundary

$$\frac{\partial \Phi_V}{\partial n_p} = -\boldsymbol{B_0} \cdot \boldsymbol{n_p}, \tag{16}$$

where $\mathbf{n_p}$ is the exterior normal vector to the plasma-vacuum interface [5, 6]. The Laplace equation can be converted to the integral relation

$$\begin{aligned} \Phi_V(\boldsymbol{x}) = & - \frac{1}{2\pi}\int d\Sigma'_p \frac{\partial G(\boldsymbol{x},\boldsymbol{x}')}{\partial n'_p}\Phi_V(\boldsymbol{x}') \\ & + \frac{1}{2\pi}\int d\Sigma'_p G(\boldsymbol{x},\boldsymbol{x}')\frac{\partial \Phi_V(\boldsymbol{x}')}{\partial n'_p}, \end{aligned} \tag{17}$$

where $\boldsymbol{x}$ and $\boldsymbol{x}'$ are points on the boundary labelled as Σ_p and $G(\boldsymbol{x},\boldsymbol{x}') = 1/|\boldsymbol{x}-\boldsymbol{x}'|$ corresponds to the Green's function. A more detailed description of the vacuum treatment adopted can be found in Refs. [5, 6]. Finally, the continuity of the total pressure across the plasma-vacuum interface must be satisfied, namely

$$p_\perp + \frac{B^2}{2\mu_0} = \frac{B_V^2}{2\mu_0}. \tag{18}$$

5. Radial force balance diagnostic

The magnetohydrodynamic force balance relation within the plasma for anisotropic pressure reduces to

$$\boldsymbol{F} = -\frac{\partial p_\parallel}{\partial s}\bigg|_B \boldsymbol{\nabla} s + \boldsymbol{K} \times \boldsymbol{B} \tag{19}$$

The derivative of the parallel pressure with respect to s is evaluated at fixed B. The flux surface average of the radial component of this relation constitutes a diagnostic that very usefully ascertains the quality of the equilibrium state that is achieved, namely

$$\left\langle \frac{F_s}{\Phi'(s)} \right\rangle = -\left\langle \frac{1}{\Phi'(s)}\frac{\partial p_\parallel}{\partial s}\bigg|_B \right\rangle - \frac{\partial}{\partial s}\left\langle \frac{\sigma B_v}{\sqrt{g}} \right\rangle - \iota(s)\frac{\partial}{\partial s}\left\langle \frac{\sigma B_u}{\sqrt{g}} \right\rangle \tag{20}$$

where B_u and B_v are the poloidal and toroidal components of the magnetic field in the covariant representation, respectively and prime ($'$) indicates the derivative of a flux surface quantity with respect to s.

6. Application to a 2-period quasiaxisymmetric stellarator reactor

A 2-field period quasiaxisymmetric stellarator reactor [22, 23] is chosen as a testbed system to investigate free boundary anisotropic pressure equilibria. We specifically concentrate on off-axis hot particle deposition on the high magnetic field (HF) with $B_C = 4.9T$ and the low field (LF) side with $B_C = 4.2T$. These conditions provide a very meaningful evaluation of the versatility of the code as we can anticipate significant poloidal localisation of the energetic particle pressure distributions particularly with large perpendicular pressure anisotropy as has been previously demonstrated in fixed boundary computations [9]. We define the volume averaged thermal β as $\langle\beta_{th}\rangle = \int_V d^3x 2\mu_0 p / \int_V d^3x B^2$ and the volume averaged total beta as $\langle\beta\rangle = \int_V d^3x \mu_0(p_{||} + p_\perp) / \int_V d^3x B^2$. The volume averaged hot particle parallel component of $\langle\beta\rangle$ is $\left\langle\beta^h_{||}\right\rangle = \int_V d^3x 2\mu_0 p_{||} / \int_V d^3x B^2 - \langle\beta_{th}\rangle$. That for $\left\langle\beta^h_{\perp}\right\rangle$ is equivalent with $p_{||}$ replaced by $p_\perp$. The thermal pressure in the calculations we have performed is prescribed as $p(s) = p(0)(1-s)(1-s^4)$. The hot particle pressure scale factor is chosen as $p_h(s) = p_{\mathcal{H}} s(1-s)$ to produce hollow fast particle parallel and perpendicular pressure profiles with maximum value around $s \sim 0.25$. Typical profiles that we have examined are presented in Fig. 2 . In principle, the ratio of energetic particle perpendicular to parallel temperature $T_\perp/T_{||}$ is a flux surface quantity, but for simplicity we have chosen it as a constant. Similarly, the critical field B_C can also vary across the flux surfaces, but we have kept this parameter as a constant which can be expected at a resonance for radio frequency wave deposition. Finally, the toroidal plasma current enclosed within each flux surface is prescribed as vanishing.

The finite β calculations we have undertaken are all at fixed $\langle\beta\rangle \simeq 4.5\%$ with a thermal component $\langle\beta_{th}\rangle \simeq 2.87\%$. We treat four separate cases

1. HF deposition ($B_C = 4.9T$), $p_\perp > p_{||}$
2. HF deposition ($B_C = 4.9T$), $p_{||} > p_\perp$
3. LF deposition ($B_C = 4.2T$), $p_\perp > p_{||}$

4. LF deposition ($B_C = 4.2T$), $p_{||} > p_{\perp}$

The cases with $p_{\perp} > p_{||}$ have $\left\langle \beta_{\perp}^{h} \right\rangle / \left\langle \beta_{||}^{h} \right\rangle \simeq 3.4$ while those with $p_{||} > p_{\perp}$ have $\left\langle \beta_{\perp}^{h} \right\rangle / \left\langle \beta_{||}^{h} \right\rangle \simeq 1/3.4$.

The coils for the quasiaxisymmetric stellarator device investigated are described with a 10-filament model per field period that carry a current of $16.2MA$ each and is shown in Fig. 3. The Biot-Savart law is applied to compute the vacuum magnetic field components in a rectangular toroidal structure enclosed within the coils. We also display in Fig. 3 the mod-B distribution on a toroidal surface corresponding to the edge of the plasma (the darker shade represents the minima of B).

An important benchmark for the accuracy of a 3D equilibrium code is to reproduce the vacuum magnetic flux surfaces of a stellarator. The dotted points in Fig. 4 correspond to Poincaré plots of the magnetic field as it traverses one of four cross sections within a field period computed with a magnetic field line tracing code. The solid contours correspond to the vacuum magnetic flux surfaces obtained with the equilibrium code. The agreement is very good with some small discrepancies at the tips of the elongated cross sections near the edge.

The main difference between fixed and free boundary equilibrium calculations is that the plasma-vacuum interface position and shape can change with finite pressure and plasma current when the boundary is allowed to move. We can see in Fig. 5 a significant outward shift of the plasma column away from the major axis when $\langle \beta \rangle \simeq 4.5\%$ compared with that of the vacuum. The shape of the boundary flux surface also changes with the tips of the elongated cross sections becoming sharper. The differences between the HF deposition, the LF deposition, the $p_{||} > p_{\perp}$ and the $p_{\perp} > p_{||}$ cases examined shows that the plasma-vacuum interface remains more or less the same with the plasma volume. The toroidal magnetic flux is fixed at $2\pi\Phi_e = 120.4Wb$.

A magnetohydrodynamic equilibrium state is achieved when the forces F_R, F_Z and F_λ vanish. The volume averaged value of the horizontal force F_R as a function of the num-

ber of iterations is shown in Fig. 6 for the configuration examined with LF hot particle deposition having $p_\perp > p_{||}$ and $\langle\beta\rangle \simeq 4.5\%$ which corresponds to the slowest converging case that we have treated. The preconditioning algorithm is activated when the averaged value of F_R drops below 1×10^{-9} which occurs after 6440 iterations. After an initial transient jump, the residual horizontal force decreases from 10^{-9} to almost 10^{-18} within 12 iterations. Fewer than 3500 iterations are required to converge the remaining finite β cases we have investigated. To verify whether this level of force is tolerable, we then evaluate the flux surface averaged radial force balance given by Eqn. (20). We normalise the expression for the radial force balance by dividing it by the sum of the absolute values of the components depicted in Eqn. (20) and then we evaluate its absolute value for plotting purposes. For comparative purposes, we show in Fig. 7 the flux surface averaged radial force balance errors for the equilibrium state (LF $p_\perp > p_{||}$, $\langle\beta\rangle \simeq 4.5\%$) computed with an old version of VMEC [6] where the model described was first implemented, with ANIMEC just before the preconditioning is turned on and with the preconditioned ANIMEC result. We obtain an order of magnitude improvement between the old VMEC code and the non-preconditioned ANIMEC code with respect to the averaged radial force balance error and another 3-4 orders of magnitude reduction with preconditioning. The absolute values of the normalised averaged radial force balance profiles for the finite β cases treated are displayed in Fig. 8. The force balance error remains below 0.0001% for all the cases considered, the worst corresponding to HF deposition with $p_\perp > p_{||}$ where the error levels remain below 1×10^{-8} within the plasma interior and climbs to just below 1×10^{-6} close to the plasma edge. These levels of radial force balance achieved are more than acceptable for magnetohydrodynamic stability and orbit analysis applications.

Charge conservation constitutes another useful diagnostic for the quality of an equilibrium state. For the anisotropic pressure model we investigate, this requires that $\boldsymbol{\nabla} \cdot \boldsymbol{K} = 0$. This condition is not required in the computation of the equilibrium. We extend the charge conservation analysis of Ref. [24] to anisotropic pressure plasmas in the

Boozer coordinate frame. The Fourier amplitudes of $\sqrt{g}(\boldsymbol{\nabla}\cdot\boldsymbol{K})$ can be written as

$$[\sqrt{g}(\boldsymbol{\nabla}\cdot\boldsymbol{K})]_{m_B n_B} = \left[\frac{m_B I(s) - n_B J(s)}{\sigma\sqrt{g}B^2}\right] \qquad \left\{\left(\sqrt{g}\frac{\partial p_{\|}}{\partial s}\bigg|_B\right)_{m_B n_B} - \; [m_B\psi'(s) - n_B\Phi'(s)](\sigma B_s)_{m_B n_B}\right\}, \quad (21)$$

where m_B and n_B are the poloidal and toroidal mode numbers in Boozer coordinates. Larger values of m_B and n_B are needed to recover the equilibrium state compared with the spectrum of the optimal coordinates used in ANIMEC and VMEC. The Fourier amplitude of Eqn. (21) for $m_B = 8$, $n_B = 2$ is displayed in Fig. 9. It shows that the best results occur when the maximum poloidal mode number used in the ANIMEC calculation is between 8 and 9. Matrix preconditioning does not significantly alter the solution. We believe this is due to errors in the transformation of coordinates, but must be verified in the future.

The vacuum and finite β rotational transform profiles for the free boundary quasiaxisymmetric stellarator equilibria are examined in Fig. 10. Finite β effects reduce the value of the rotational transform quite significantly in the absence of a driven or a bootstrap current. Large parallel anisotropy decreases the rotational transform by a slightly larger fraction than perpendicular anisotropy. The $p_{||} > p_{\perp}$ rotational transform profiles align more closely with each other than the corresponding $p_{\perp} > p_{||}$ profiles. The differential volume profiles for the vacuum and the $\langle\beta\rangle \simeq 4.5\%$ cases are plotted in Fig. 11. The vacuum case has a weak magnetic well ($dV/d\Phi < 0$) which deepens significantly in the outer 3/4 fraction of the plasma volume with finite β. With the hollow fast particle profiles considered, the inner 20% of the plasma volume develops a magnetic hill. The $dV/d\Phi$ profiles at finite β align very closely one with another except for the LF side $p_{\perp} > p_{||}$ case which has a stronger inner magnetic hill and a deeper well between one quarter and half the plasma volume.

In Fig. 12, we present the contours of constant hot particle perpendicular pressure $p_{\perp}^h$ (top row) of constant fast particle parallel pressure $p_{||}^h$ (middle row) and of constant

modulus of the magnetic field strength B for the case of HF side hot particle deposition ($B_C = 4.9T$) and $p_\perp > p_{||}$ on three cross sections that span half of a field period in the quasiaxisymmetric stellarator reactor. We undertake a comparative analysis of the localisation of the fast particle pressure distributions at $\langle\beta\rangle \simeq 4.5\%$ for the cases we investigate by concentrating on the up-down symmetric cross section at midperiod ($v = \pi/2$). For the cases with $\left\langle\beta^h_\perp\right\rangle / \left\langle\beta^h_{||}\right\rangle \simeq 3.4$, the $p^h_\perp$ is peaked at, and the contours concentrate in an annular domain on the HF(LF) side for HF(LF) hot particle deposition as shown in Fig. 13. On the other hand, in Fig. 14, the $p^h_{||}$ contours are localised on the low field side regardless of the position of the fast particle deposition layer. For the cases with large parallel pressure anisotropy ($\left\langle\beta^h_\perp\right\rangle / \left\langle\beta^h_{||}\right\rangle \simeq 1/3.4$), both the $p^h_\perp$ and the $p^h_{||}$ contours remain more or less uniform around the flux surfaces with a slight tilt towards the high field side as displayed in Fig. 15 for $p^h_\perp$ and Fig. 16 for $p^h_{||}$.

7. Summary and conclusions

A free boundary version of the 3D VMEC code [6] combined with the NESTOR code [5] has been modified to compute anisotropic equilibria with nested magnetic flux surfaces (called the ANIMEC code). The energetic particle pressure moments are calculated analytically from the variant of a bi-Maxwellian distribution function that satisfies the constraint $\boldsymbol{B}\cdot\boldsymbol{\nabla}\mathcal{F}_h = 0$ consistent with the lowest order solution of the Fokker-Planck equation. A steepest descent energy minimisation procedure of the functional $W = \int_V d^3x[B^2/(2\mu_0) + p_{||}/(\Gamma - 1)]$ coupled with a preconditioning algorithm to improve convergence is applied to compute the minimal energy state. A Green's function method is employed to determine the magnetic field at the plasma-vacuum interface with the condition that its normal component at the boundary surface vanishes and the total pressure $p_\perp + B^2/(2\mu_0)$ is continuous across the interface.

We have concentrated the applications to a comparative study of off-axis high and

low field side energetic particle deposition with large parallel and perpendiuclar pressure anisotropy at $\langle\beta\rangle \simeq 4.5\%$ with zero net toroidal current enclosed within each flux surface in a 2-period quasiaxisymmetric stellarator reactor system. As a first step, we have verified that the equilibrium calculation recovers that vacuum flux surfaces obtained from magnetic field line tracing. At finite β, the entire plasma column shifts significantly away from the major axis. The flux surface shapes are altered with finite pressure particularly near the tips of the elongated cross sections, but the variation is minimal with respect to changes in the ratio of $p_\perp$ to $p_{||}$ at finite β.

Under current-free conditions, the rotational transform decreases markedly with finite β. This decrease is somewhat larger for $p_{||} > p_\perp$. The magnetic well at finite β becomes stronger in the outer 75% of the plasma volume, but develops a hill in the inner 20%, however the effects of $p_\perp \neq p_{||}$ though visible, are small. For $\left\langle\beta_\perp^h\right\rangle / \left\langle\beta_{||}^h\right\rangle \simeq 1/3.4$, $(p_{||} > p_\perp)$, the hot particle pressure contours do not differ significantly whether high field or low field side energetic particle deposition is applied and the pressures remain more or less uniform on a flux surface. On the other hand for $\left\langle\beta_\perp^h\right\rangle / \left\langle\beta_{||}^h\right\rangle \simeq 3.4$, $(p_\perp > p_{||})$, the hot particle perpendicular pressure contours become localised to the regions where the energetic particle deposition occurs. This can be understood by the fact that the trapped fast particles spend most of their orbit time within the confines of the deposition layer locally enhancing the perpendicular pressure. For $p_\perp > p_{||}$, the hot particle parallel pressure localises in the low field region regardless of the position where the fast particle deposition occurs.

Acknowledgments

This research was partially sponsored by the Fonds National Suisse de la Recherche Scientifique and Euratom. One of the authors (WAC) would like to thank the hospitality of the Oak Ridge National Laboratory where a significant part of the development of the

ANIMEC code was completed.

References

[1] T. Yamaguchi, K. Y. Watanabe, S. Sakakibara, Y. Narushima, K. Narihara, T. Tokuzawa, K. Tanaka, I. Yamada, M. Osakabe, H. Yamada, K. Kawahata, K. Yamazaki and LHD experimental group, *Nucl. Fusion* **45** (2005) L33.

[2] K. Y. Watanabe, S. Sakakibara, Y. Narushima, H. Funaba, K. Narihara, K. Tanaka, T. Yamaguchi, K. Toi, S. Ohdachi, O. Kaneko, H. Yamada, Y. Suzuki, W. A. Cooper, S. Murakami, N. Nakajima, I. Yamada, K. Kawahata, T. Tokuzawa, A. Komori and LHD experimental group, *Nucl. Fusion* **45** (2005) 1247;

[3] J. P. Graves, W. A. Cooper, S. Coda, L. -G. Eriksson and JET-EFDA contributors, *in Proc. of the Joint Varenna-Lausanne International Workshop on Theory of Fusion Plasmas*, AIP Conference Proceedings Vol. 871 (2006), pp. 350-355 (*http://proceedings.aip.org/proceedings*).

[4] S. P. Hirshman and O. Betancourt, *J. Comput. Phys.* **96** (1991) 99.

[5] P. Merkel, *J. Comput. Phys.* **66** (1986) 83.

[6] S. P. Hirshman, W. I. van Rij and P. Merkel, *Comput. Phys. Commun.* **43** (1986) 143.

[7] R. W. Harvey, M. G. McCoy, G. D. Kerbel and S. C. Chiu, *Nucl. Fusion* **26** (1986) 43.

[8] K. G. McClements, R. O. Dendy, R. J. Hastie and T. J. Martin, *Phys. Plasmas* **3** (1996) 2994.

[9] W. A. Cooper, J. P. Graves, S. P. Hirshman, T. Yamaguchi, Y. Narushima, S. Okamura, S. Sakakibara, C. Suzuki, K. Y. Watanabe, H. Yamada and K. Yamazaki, Nucl. Fusion **46** (2006) 683.

[10] W. A. Cooper, G. Bateman, D. B. Nelson and T. Kammash, Nucl. Fusion **20** (1980) 985.

[11] E. Salberta, R. C. Grimm, J. L. Johnson, J. Manickam and W. M. Tang, Phys. Fluids **30** (1987) 2796.

[12] W. Zwingmann, L.-G. Eriksson and P. Stubberfield, *Plasma Phys. Control. Fusion* **43** (2001) 1441.

[13] R. L. Miller, *Phys. Fluids* **29** (1986) 1176.

[14] W. A. Cooper, S. P. Hirshman and M. C. Depassier, *Phys. Fluids* **30** (1987) 3532.

[15] W. N. G. Hitchon, *Nucl. Fusion* **23**, (1983) 383.

[16] W. A. Cooper, S. P. Hirshman, R. Gruber and S. Merazzi, *Comput. Phys. Commun.* **72** (1992) 1.

[17] W. A. Cooper, S. P. Hirshman, T. Yamaguchi, Y. Narushima, S. Okamura, S. Sakakibara, C. Suzuki, K. Y. Watanabe, H. Yamada and K. Yamazaki, *Plasma Phys. Control. Fusion* **47** (2005) 561.

[18] H. Grad, *Phys. Fluids* **9** (1966) 498.

[19] S. P. Hirshman and J. C. Whitson, *Phys. Fluids* **26** (1983) 3553.

[20] S. P. Hirshman, U. Schwenn and J. Nührenberg, *J. Comput. Phys.* **87** (1990) 396.

[21] Y. Saad and M. H. Schultz, *SIAM J. Sci. Stat. Comput.* **7** (1986) 856; V. Frayssé, L. Giraud, S. Gratton and J. Langou, *CERFACS Technical Report TR/PA/03/3, public domain software on www.cerfacs.fr/algor/Softs*, 2003

[22] S. Okamura, K. Matsuoka, M. Fujiwara, M. Drevlak, P. Merkel and J. Nührenberg, *J. Plasma Fusion Res.* **1**, 164 (1998).

[23] W. A. Cooper, S. Ferrando i Margalet, S. Allfrey, J. Kisslinger, H. F. G. Wobig, Y. Narushima, S. Okamura, C. Suzuki, K. Y. Watanabe, K. Yamazaki and M. Yu. Isaev, *Fusion Sci. Technol.* **46** (2004) 365.

[24] R. Moeckli and W. A. Cooper, *Nucl. Fusion* **33** (1993) 1899.

Figure Captions

Figure 1. Contours of constant hot particle distribution in $v_\perp$ versus $v_{||}$ space. The distribution function plotted corresponds to $\mathcal{N}(m_h/2\pi T_\perp)^{3/2}[\alpha(T_\perp/T_t)^{3/2}\exp(-m_h\mathcal{E}/T_t)+(1-\alpha)\exp(-\mu B_C/T_\perp-|\mathcal{E}-\mu B_C|/T_{||})$ where the thermal, hot particle perpendicular and hot particle parallel temperatures are T_t, $T_\perp$ and $T_{||}$, respectively. The parameters required are given by $\alpha = 0.1$, $T_\perp/T_t = 20$, $T_\perp/T_{||} = 4.2$ and $B_C/B = 1.3$.

Figure 2. The flux surface averaged thermal pressure p, the hot particle parallel pressure $p^h_{||}$ and the hot particle perpendicular pressure $p_\perp$ profiles as a function of the radial variable s (roughly proportional to volume enclosed).

Figure 3. Filament coil model for a 2-field period quasiaxisymmetric stellarator reactor and the last closed vacuum magnetic flux surface depicting the mod-B distribution. The low magnetic field side is presented in dark shade, the high magnetic field side in lighter shade.

Figure 4. A Poincaré plot computed with a magnetic field line tracing solver (green dots) and the vacuum magnetic flux surfaces calculated with the ANIMEC code on four cross section spanning three fourths of a field period in the quasiaxisymmetric stellarator.

Figure 5. The shape of the plasma-vacuum interface boundary under vacuum conditions (green curve) and at $\langle\beta\rangle \simeq 4.5\%$ for four cases a) $B_c = 4.9T$; $\left\langle\beta^h_\perp\right\rangle / \left\langle\beta^h_{||}\right\rangle \simeq 3.4$ (HF side hot particle deposition with $p_\perp > p_{||}$) (blue curve), b) $B_c = 4.2T$; $\left\langle\beta^h_\perp\right\rangle / \left\langle\beta^h_{||}\right\rangle \simeq 3.4$ (LF side hot particle deposition with $p_\perp > p_{||}$) (red curve), c) $B_c = 4.9T$; $\left\langle\beta^h_\perp\right\rangle / \left\langle\beta^h_{||}\right\rangle \simeq 1/3.4$ (HF side hot particle deposition with $p_{||} > p_\perp$), d) $B_c = 4.2T$; $\left\langle\beta^h_\perp\right\rangle / \left\langle\beta^h_{||}\right\rangle \simeq 1/3.4$ (LF side hot particle deposition with $p_{||} > p_\perp$) (black curve) on three cross sections spanning half a field period of the quasiaxisymmetric stellarator reactor. The boundaries in cases c) and d) are virtually indistinguishable and also very close to case a). Case b) bulges out at the elongated up-down symmetric cross section.

Figure 6. The volume average of the residual horizontal force F_R as a function of the number of iterations for the case at $\langle\beta\rangle \simeq 4.5\%$ corresponding to $B_c = 4.2T$ and

$\left\langle \beta_{\perp}^{h} \right\rangle / \left\langle \beta_{||}^{h} \right\rangle \simeq 3.4$ in a 2-field period quasiaxisymmetric stellarator reactor.The preconditioning algorithm is turned on after 6440 iterations.

Figure 7. The absolute values of the flux surface averaged radial force balance profiles for a 2-field period quasiaxisymmetric stellarator reactor system with off-axis hot particle deposition at $\langle\beta\rangle \simeq 4.5\%$ corresponding to $B_c = 4.2T$; $\left\langle \beta_{\perp}^{h} \right\rangle / \left\langle \beta_{||}^{h} \right\rangle \simeq 3.4$ (LF side hot particle deposition with $p_{\perp} > p_{||}$), computed with an old version of VMEC (black curve), with ANIMEC without matrix preconditioning (blue curve) and with the preconditioned ANIMEC code (red curve).

Figure 8. The absolute values of the flux surface averaged radial force balance profiles for a 2-field period quasiaxisymmetric stellarator reactor system with off-axis hot particle deposition at $\langle\beta\rangle \simeq 4.5\%$. The cases investigated have a) $B_c = 4.9T$; $\left\langle \beta_{\perp}^{h} \right\rangle / \left\langle \beta_{||}^{h} \right\rangle \simeq 3.4$ (HF side hot particle deposition with $p_{\perp} > p_{||}$) (blue curve), b) $B_c = 4.2T$; $\left\langle \beta_{\perp}^{h} \right\rangle / \left\langle \beta_{||}^{h} \right\rangle \simeq 3.4$ (LF side hot particle deposition with $p_{\perp} > p_{||}$) (red curve), c) $B_c = 4.9T$; $\left\langle \beta_{\perp}^{h} \right\rangle / \left\langle \beta_{||}^{h} \right\rangle \simeq 1/3.4$ (HF side hot particle deposition with $p_{||} > p_{\perp}$) (magenta curve), d) $B_c = 4.2T$; $\left\langle \beta_{\perp}^{h} \right\rangle / \left\langle \beta_{||}^{h} \right\rangle \simeq 1/3.4$ (LF side hot particle deposition with $p_{||} > p_{\perp}$) (black curve).

Figure 9. Convergence of the $m_B = 8$, $n_B = 2$ Fourier component of $\sqrt{g}(\boldsymbol{\nabla} \cdot \boldsymbol{K})$ in the Boozer coordinate frame as a function of the inverse of the maximum value of the poloidal mode number m used in the equilibrium computation for the case $B_c = 4.9T$; $\left\langle \beta_{\perp}^{h} \right\rangle / \left\langle \beta_{||}^{h} \right\rangle \simeq 3.4$ (HF side hot particle deposition with $p_{\perp} > p_{||}$) in a 2-period quasiaxisymmetric stellarator. The ordinate has not been normalised so its units are A/m.

Figure 10. The vacuum (green curve) and the finite $\langle\beta\rangle \simeq 4.5\%$ rotational transform profiles in a 2-field period quasiaxisymmetric stellarator system with off-axis energetic particle deposition. The finite β cases investigated have a) $B_c = 4.9T$; $\left\langle \beta_{\perp}^{h} \right\rangle / \left\langle \beta_{||}^{h} \right\rangle \simeq 3.4$ (HF side hot particle deposition with $p_{\perp} > p_{||}$) (blue curve), b) $B_c = 4.2T$; $\left\langle \beta_{\perp}^{h} \right\rangle / \left\langle \beta_{||}^{h} \right\rangle \simeq 3.4$ (LF side hot particle deposition with $p_{\perp} > p_{||}$) (red curve), c) $B_c = 4.9T$; $\left\langle \beta_{\perp}^{h} \right\rangle / \left\langle \beta_{||}^{h} \right\rangle \simeq 1/3.4$ (HF side hot particle deposition with $p_{||} > p_{\perp}$), d) $B_c = 4.2T$; $\left\langle \beta_{\perp}^{h} \right\rangle / \left\langle \beta_{||}^{h} \right\rangle \simeq 1/3.4$ (LF side hot particle deposition with $p_{||} > p_{\perp}$) (black curve). The curves with $p_{||} > p_{\perp}$ lay

approximately on top of one another.

Figure 11. The vacuum (green line) and the finite $\langle\beta\rangle \simeq 4.5\%$ differential volume profiles in a 2-field period quasiaxisymmetric stellarator system with off-axis energetic particle deposition. The finite β cases investigated have a) $B_c = 4.9T$; $\left\langle\beta_{\perp}^{h}\right\rangle / \left\langle\beta_{||}^{h}\right\rangle \simeq 3.4$ (HF side hot particle deposition with $p_{\perp} > p_{||}$) (blue curve), b) $B_c = 4.2T$; $\left\langle\beta_{\perp}^{h}\right\rangle / \left\langle\beta_{||}^{h}\right\rangle \simeq 3.4$ (LF side hot particle deposition with $p_{\perp} > p_{||}$) (red curve), c) $B_c = 4.9T$; $\left\langle\beta_{\perp}^{h}\right\rangle / \left\langle\beta_{||}^{h}\right\rangle \simeq 1/3.4$ (HF side hot particle deposition with $p_{||} > p_{\perp}$), d) $B_c = 4.2T$; $\left\langle\beta_{\perp}^{h}\right\rangle / \left\langle\beta_{||}^{h}\right\rangle \simeq 1/3.4$ (LF side hot particle deposition with $p_{||} > p_{\perp}$) (black curve). The curves with $p_{||} > p_{\perp}$ lay approximately on top of one another.

Figure 12. The contours of constant hot particle perpendicular pressure $p_{\perp}^{h}$ (top row), hot particle parallel pressure $p_{||}^{h}$ (middle row) and the mod-B (bottom row) in a 2-field period quasiaxisymmetric stellarator reactor system with high field side energetic particle deposition at $\langle\beta\rangle \simeq 4.5\%$ with large perpendicular anisotropy ($p_{\perp} > p_{||}$) corresponding to $\left\langle\beta_{\perp}^{h}\right\rangle / \left\langle\beta_{||}^{h}\right\rangle \simeq 3.4$ on three cross sections spanning half of a field period.

Figure 13. The hot particle perpendicular pressure $p_{\perp}^{h}$ contours for $p_{\perp} > p_{||}$ HF side deposition ($B_C = 4.9T$; $\left\langle\beta_{\perp}^{h}\right\rangle / \left\langle\beta_{||}^{h}\right\rangle \simeq 3.4$) (left) and $p_{\perp} > p_{||}$ LF side deposition ($B_C = 4.2T$; $\left\langle\beta_{\perp}^{h}\right\rangle / \left\langle\beta_{||}^{h}\right\rangle \simeq 3.4$) (right) at midperiod in a 2-field period quasiaxisymmetric stellarator reactor at $\langle\beta\rangle \simeq 4.5\%$.

Figure 14. The hot particle parallel pressure $p_{||}^{h}$ contours for $p_{\perp} > p_{||}$ HF side deposition ($B_C = 4.9T$; $\left\langle\beta_{\perp}^{h}\right\rangle / \left\langle\beta_{||}^{h}\right\rangle \simeq 3.4$) (left) and $p_{\perp} > p_{||}$ LF side deposition ($B_C = 4.2T$; $\left\langle\beta_{\perp}^{h}\right\rangle / \left\langle\beta_{||}^{h}\right\rangle \simeq 3.4$) (right) at midperiod in a 2-field period quasiaxisymmetric stellarator reactor at $\langle\beta\rangle \simeq 4.5\%$.

Figure 15. The hot particle perpendicular pressure $p_{\perp}^{h}$ contours for $p_{||} > p_{\perp}$ HF side deposition ($B_C = 4.9T$; $\left\langle\beta_{\perp}^{h}\right\rangle / \left\langle\beta_{||}^{h}\right\rangle \simeq 1/3.4$) (left) and $p_{||} > p_{\perp}$ LF side deposition ($B_C = 4.2T$; $\left\langle\beta_{\perp}^{h}\right\rangle / \left\langle\beta_{||}^{h}\right\rangle \simeq 1/3.4$) (right) at midperiod in a 2-field period quasiaxisymmetric stellarator reactor at $\langle\beta\rangle \simeq 4.5\%$.

Figure 16. The hot particle parallel pressure $p_{||}^{h}$ contours for $p_{||} > p_{\perp}$ HF side deposition

($B_C = 4.9T$; $\left\langle \beta_\perp^h \right\rangle / \left\langle \beta_{||}^h \right\rangle \simeq 1/3.4$) (left) and $p_{||} > p_\perp$ LF side deposition ($B_C = 4.2T$; $\left\langle \beta_\perp^h \right\rangle / \left\langle \beta_{||}^h \right\rangle \simeq 1/3.4$) (right) at midperiod in a 2-field period quasiaxisymmetric stellarator reactor at $\langle \beta \rangle \simeq 4.5\%$.

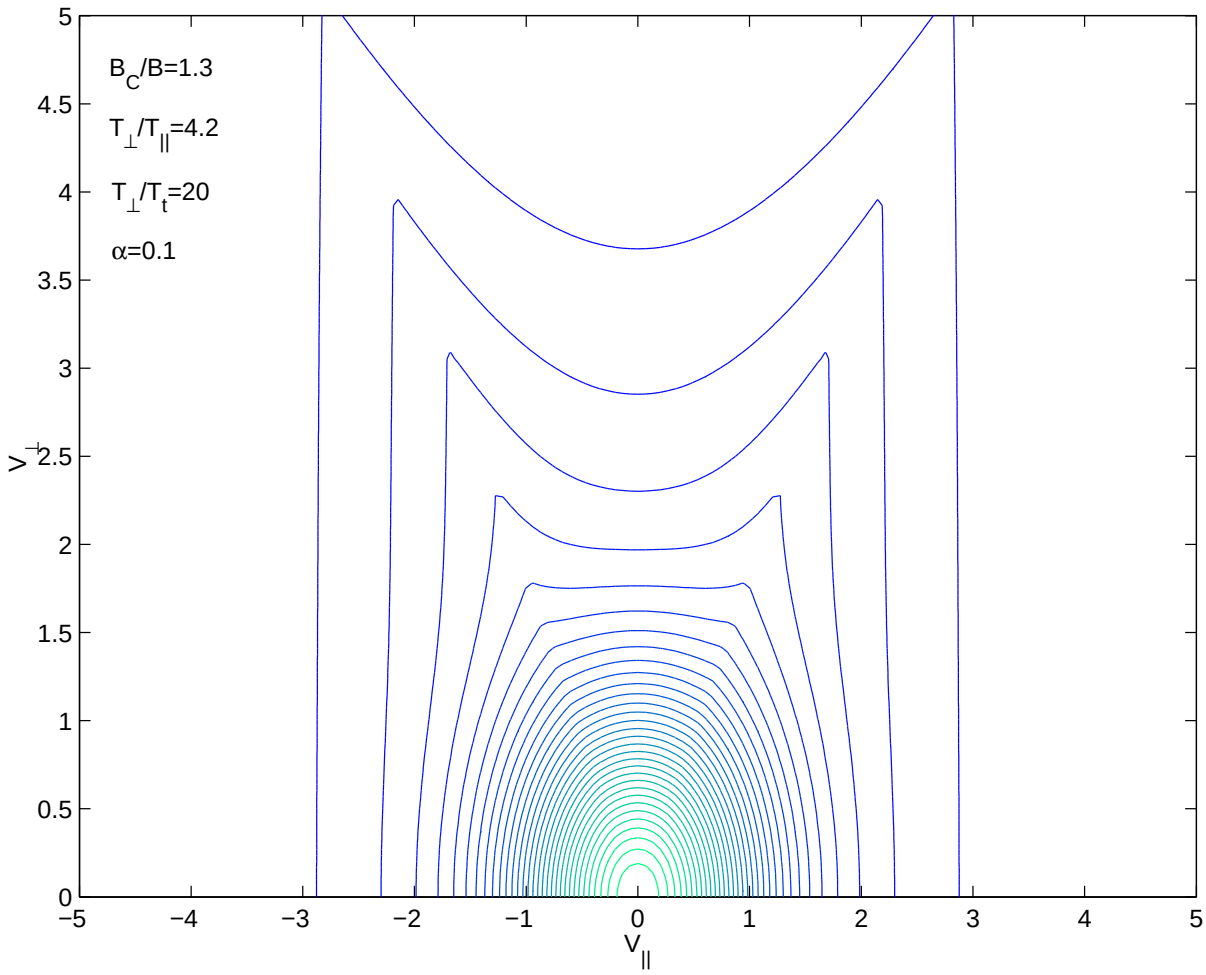

Figure 1: Contours of constant hot particle distribution in $v_\perp$ versus $v_{||}$ space. The distribution function plotted corresponds to $\mathcal{N}(m_h/2\pi T_\perp)^{3/2}[\alpha(T_\perp/T_t)^{3/2}\exp(-m_h\mathcal{E}/T_t)+(1-\alpha)\exp(-\mu B_C/T_\perp-|\mathcal{E}-\mu B_C|/T_{||})$ where the thermal, hot particle perpendicular and hot particle parallel temperatures are T_t, $T_\perp$ and $T_{||}$, respectively. The parameters required are given by $\alpha = 0.1$, $T_\perp/T_t = 20$, $T_\perp/T_{||} = 4.2$ and $B_C/B = 1.3$.

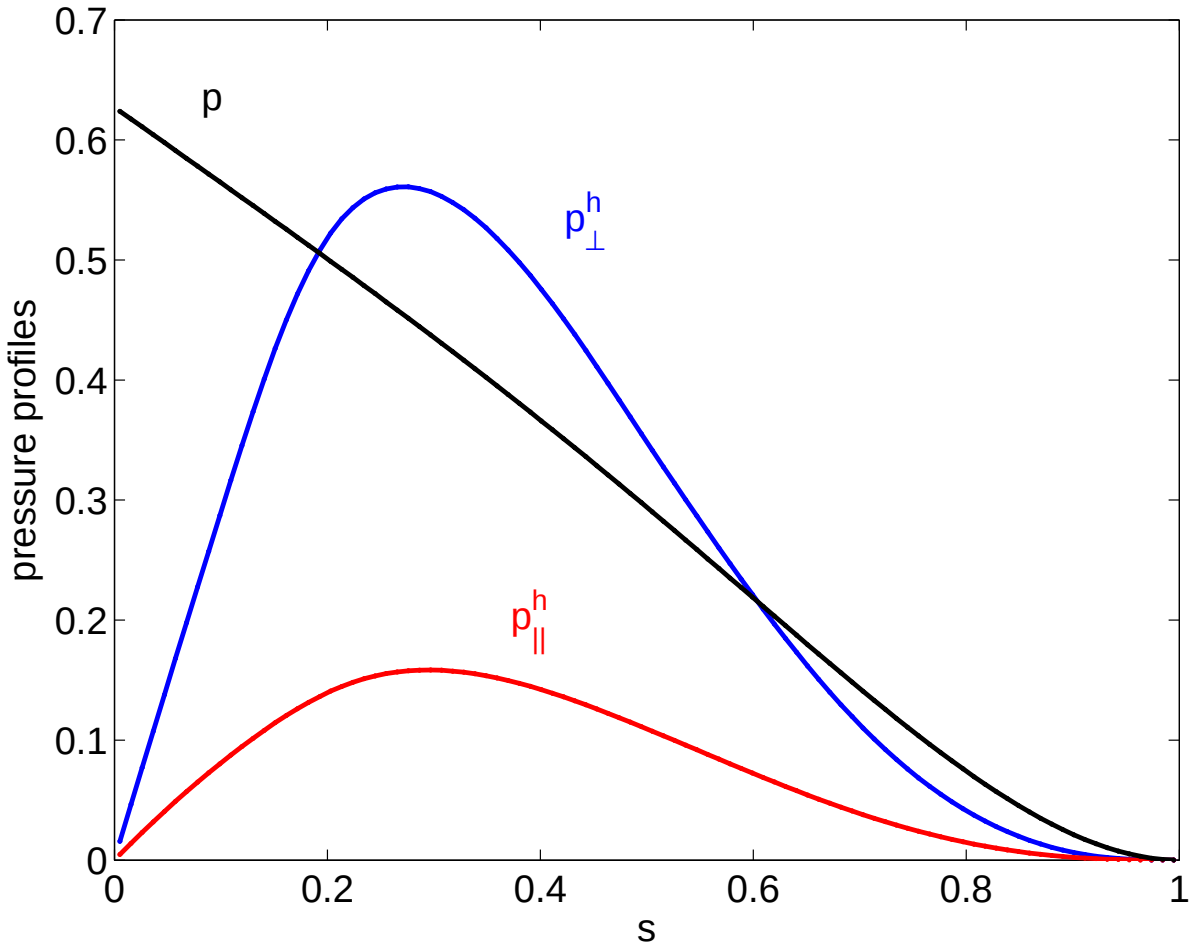

Figure 2: The flux surface averaged thermal pressure p, the hot particle parallel pressure $p^h_{||}$ and the hot particle perpendicular pressure $p_\perp$ profiles as a function of the radial variable s (roughly proportional to volume enclosed). cp

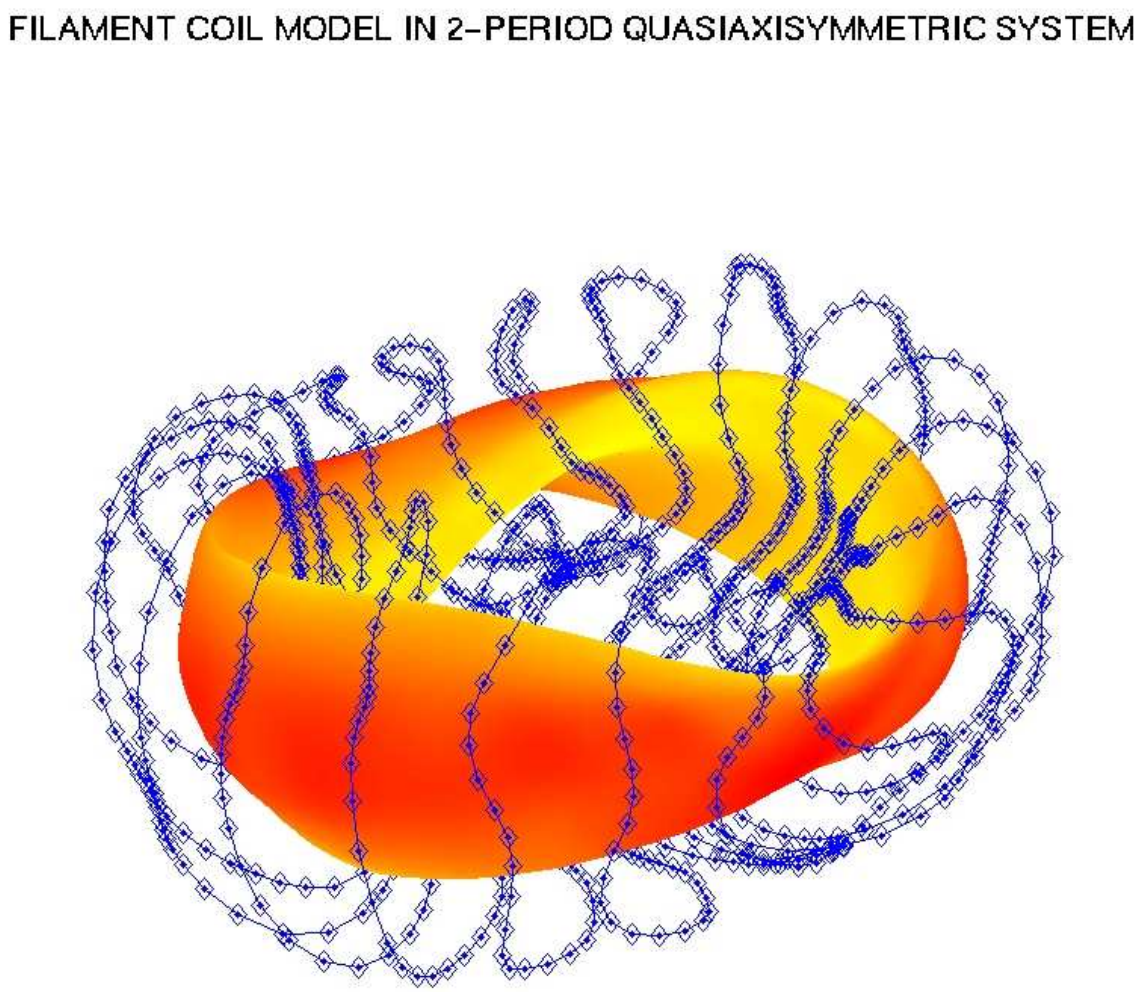

Figure 3: Filament coil model for a 2-field period quasiaxisymmetric stellarator reactor and the last closed vacuum magnetic flux surface depicting the mod-B distribution. The low magnetic field side is presented in dark shade, the high magnetic field side in lighter shade.

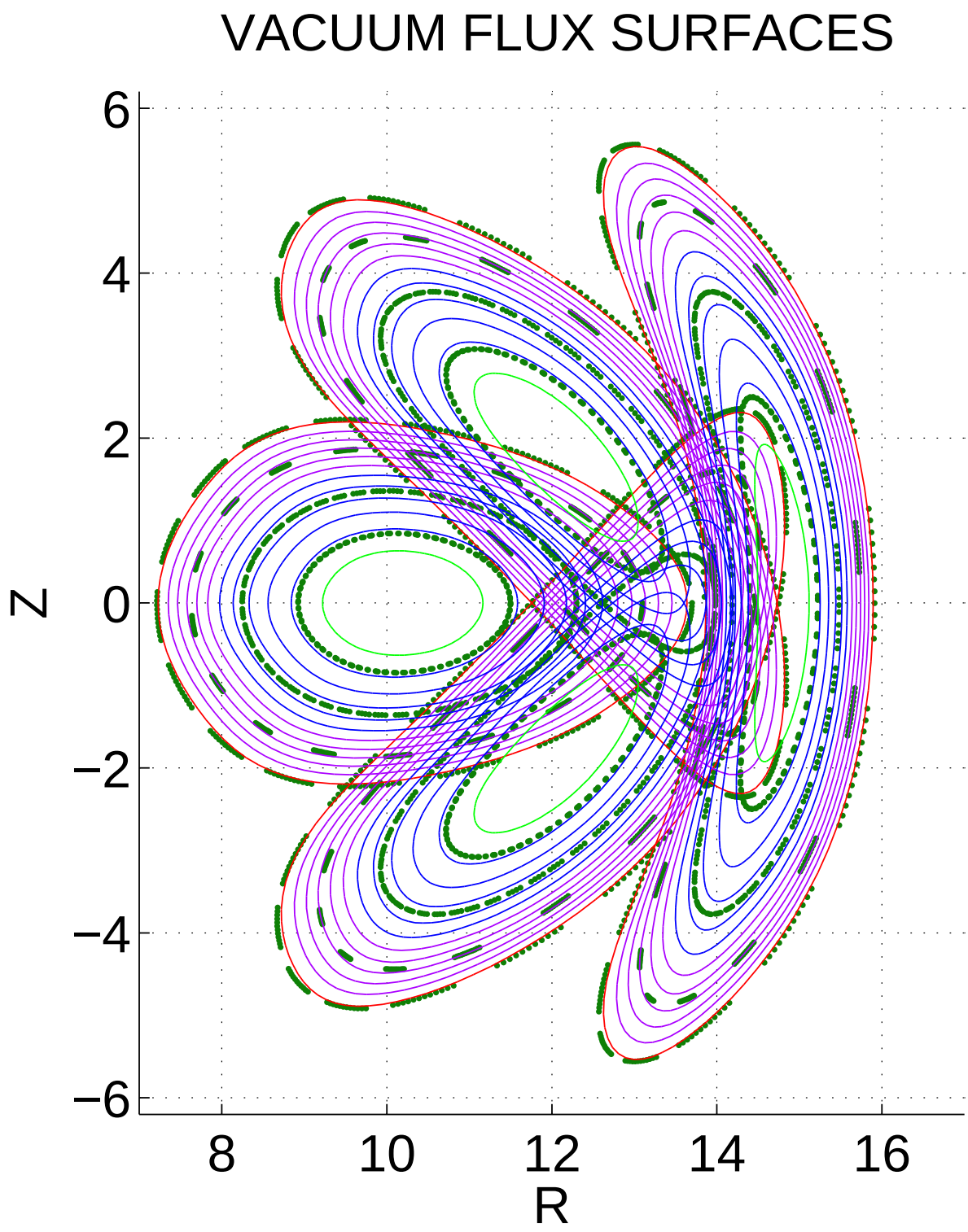

Figure 4: A Poincaré plot computed with a magnetic field line tracing solver (green dots) and the vacuum magnetic flux surfaces calculated with the ANIMEC code on four cross section spanning three fourths of a field period in the quasiaxisymmetric stellarator.

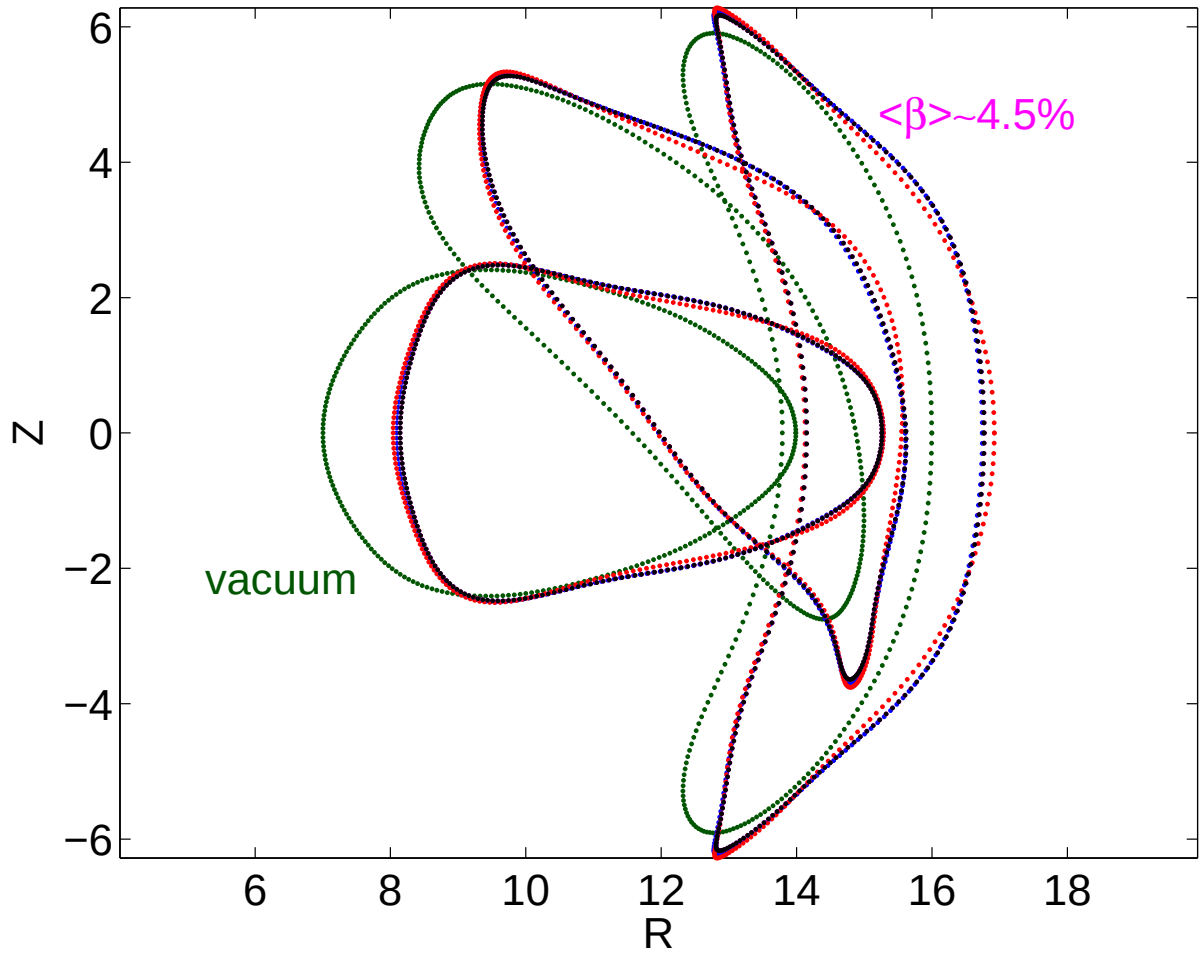

Figure 5: The shape of the plasma-vacuum interface boundary under vacuum conditions (green curve) and at $\langle\beta\rangle \simeq 4.5\%$ for four cases a) $B_c = 4.9T$; $\left\langle\beta_{\perp}^{h}\right\rangle / \left\langle\beta_{||}^{h}\right\rangle \simeq 3.4$ (HF side hot particle deposition with $p_{\perp} > p_{||}$) (blue curve), b) $B_c = 4.2T$; $\left\langle\beta_{\perp}^{h}\right\rangle / \left\langle\beta_{||}^{h}\right\rangle \simeq 3.4$ (LF side hot particle deposition with $p_{\perp} > p_{||}$) (red curve), c) $B_c = 4.9T$; $\left\langle\beta_{\perp}^{h}\right\rangle / \left\langle\beta_{||}^{h}\right\rangle \simeq 1/3.4$ (HF side hot particle deposition with $p_{||} > p_{\perp}$), d) $B_c = 4.2T$; $\left\langle\beta_{\perp}^{h}\right\rangle / \left\langle\beta_{||}^{h}\right\rangle \simeq 1/3.4$ (LF side hot particle deposition with $p_{||} > p_{\perp}$) (black curve) on three cross sections spanning half a field period of the quasiaxisymmetric stellarator reactor. The boundaries in cases c) and d) are virtually indistinguishable and also very close to case a). Case b) bulges out at the elongated up-down symmetric cross section.

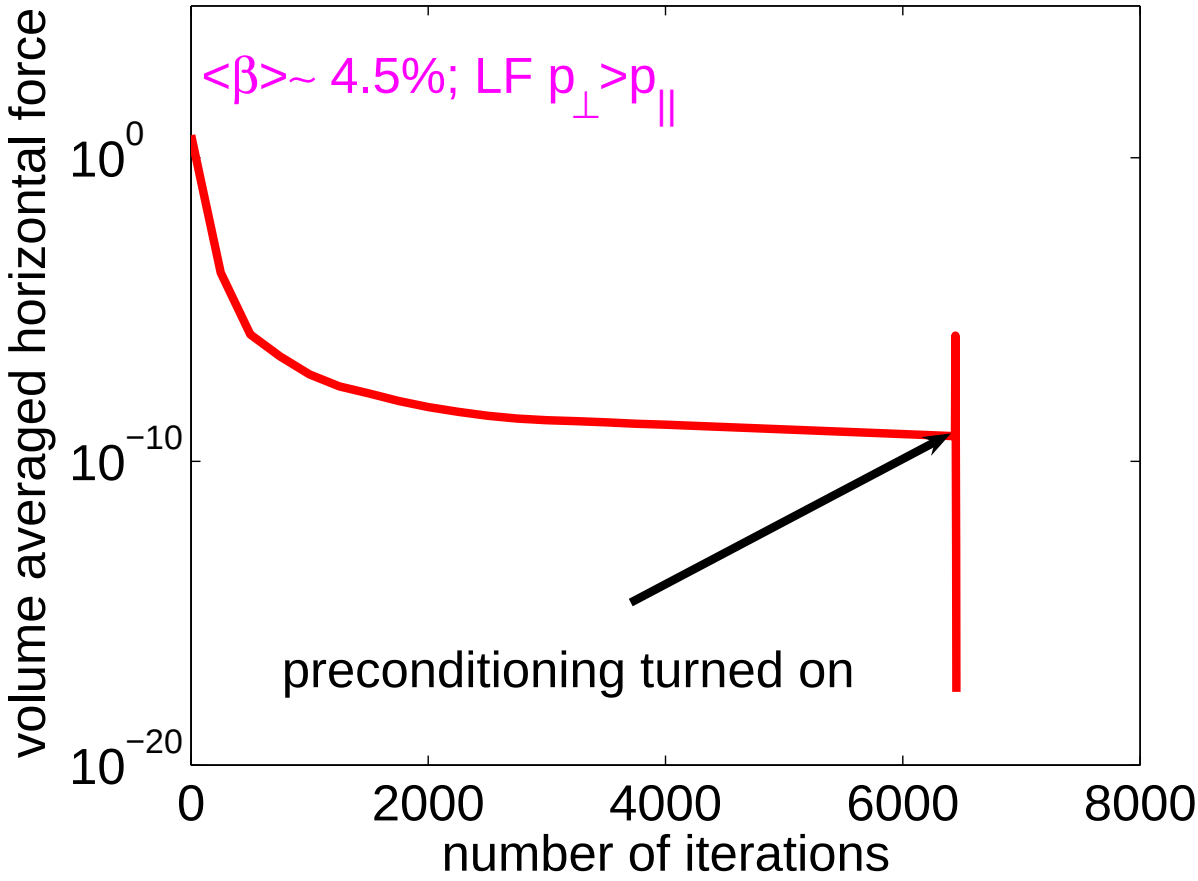

Figure 6: The volume average of the residual horizontal force F_R as a function of the number of iterations for the case at $\langle\beta\rangle \simeq 4.5\%$ corresponding to $B_c = 4.2T$ and $\left\langle\beta_{\perp}^{h}\right\rangle / \left\langle\beta_{||}^{h}\right\rangle \simeq 3.4$ in a 2-field period quasiaxisymmetric stellarator reactor.The preconditioning algorithm is turned on after 6440 iterations.

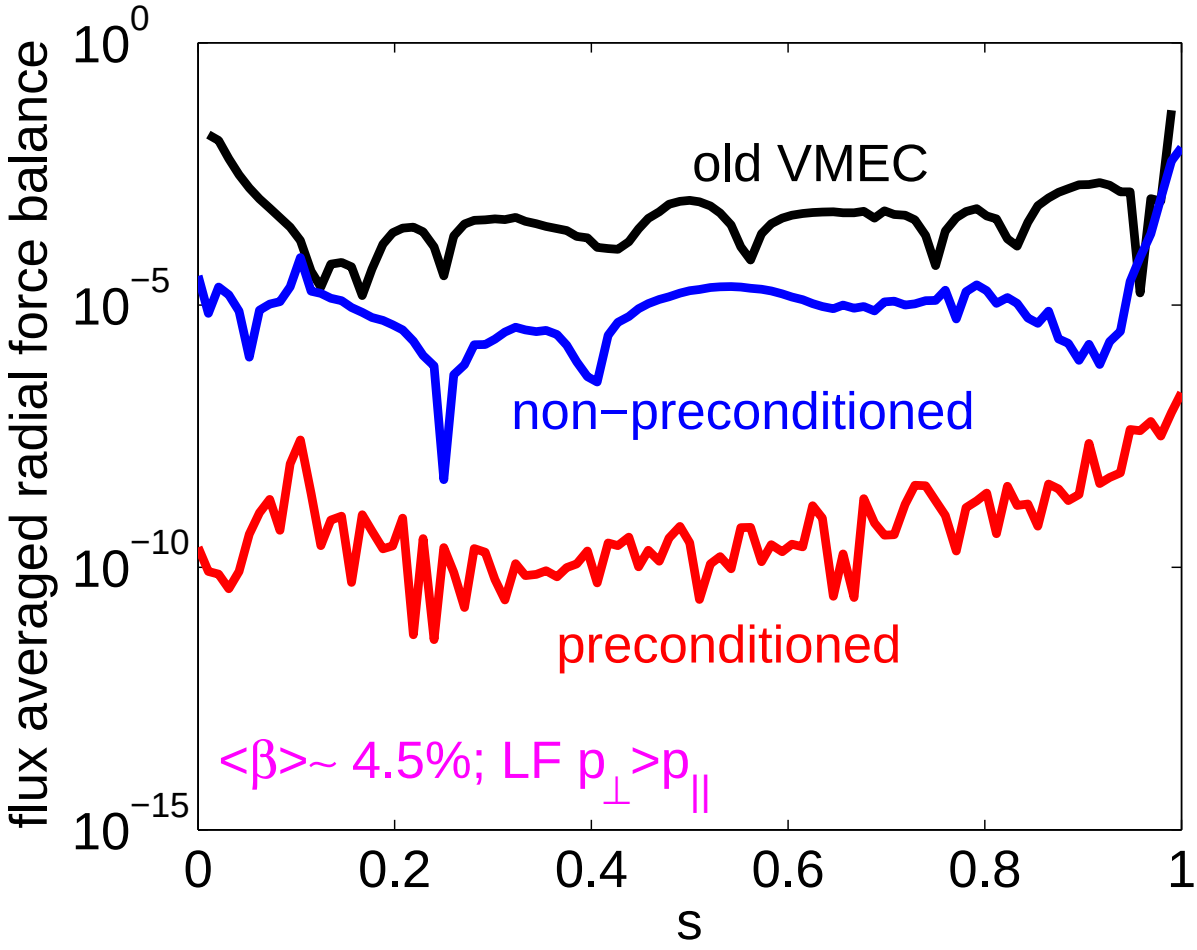

Figure 7: The absolute values of the flux surface averaged radial force balance profiles for a 2-field period quasiaxisymmetric stellarator reactor system with off-axis hot particle deposition at $\langle\beta\rangle \simeq 4.5\%$ corresponding to $B_c = 4.2T$; $\left\langle\beta_{\perp}^{h}\right\rangle / \left\langle\beta_{||}^{h}\right\rangle \simeq 3.4$ (LF side hot particle deposition with $p_{\perp} > p_{||}$), computed with an old version of VMEC (black curve), with ANIMEC without matrix preconditioning (blue curve) and with the preconditioned ANIMEC code (red curve).

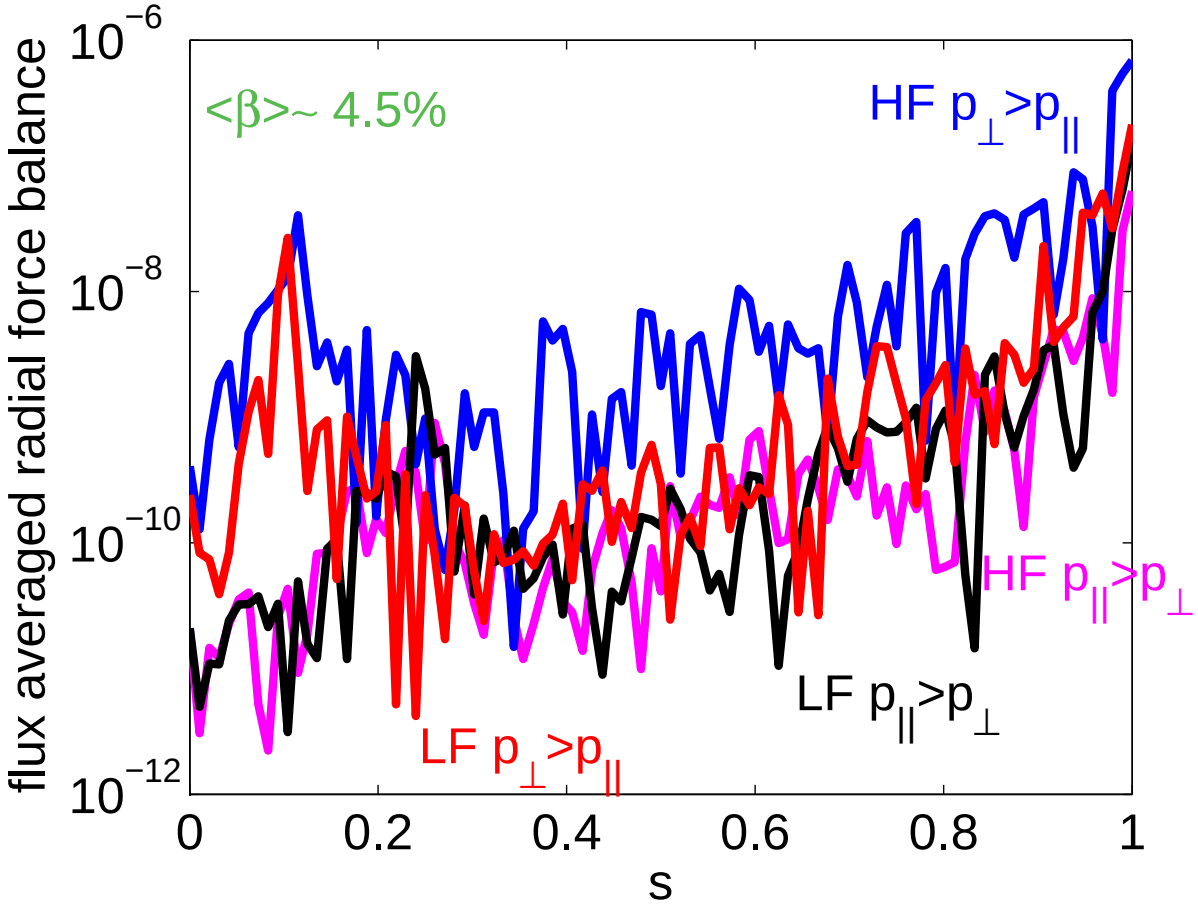

Figure 8: The absolute values of the flux surface averaged radial force balance profiles for a 2-field period quasiaxisymmetric stellarator reactor system with off-axis hot particle deposition at $\langle\beta\rangle \simeq 4.5\%$. The cases investigated have a) $B_c = 4.9T$; $\left\langle\beta_\perp^h\right\rangle / \left\langle\beta_{||}^h\right\rangle \simeq 3.4$ (HF side hot particle deposition with $p_\perp > p_{||}$) (blue curve), b) $B_c = 4.2T$; $\left\langle\beta_\perp^h\right\rangle / \left\langle\beta_{||}^h\right\rangle \simeq 3.4$ (LF side hot particle deposition with $p_\perp > p_{||}$) (red curve), c) $B_c = 4.9T$; $\left\langle\beta_\perp^h\right\rangle / \left\langle\beta_{||}^h\right\rangle \simeq 1/3.4$ (HF side hot particle deposition with $p_{||} > p_\perp$) (magenta curve), d) $B_c = 4.2T$; $\left\langle\beta_\perp^h\right\rangle / \left\langle\beta_{||}^h\right\rangle \simeq 1/3.4$ (LF side hot particle deposition with $p_{||} > p_\perp$) (black curve).

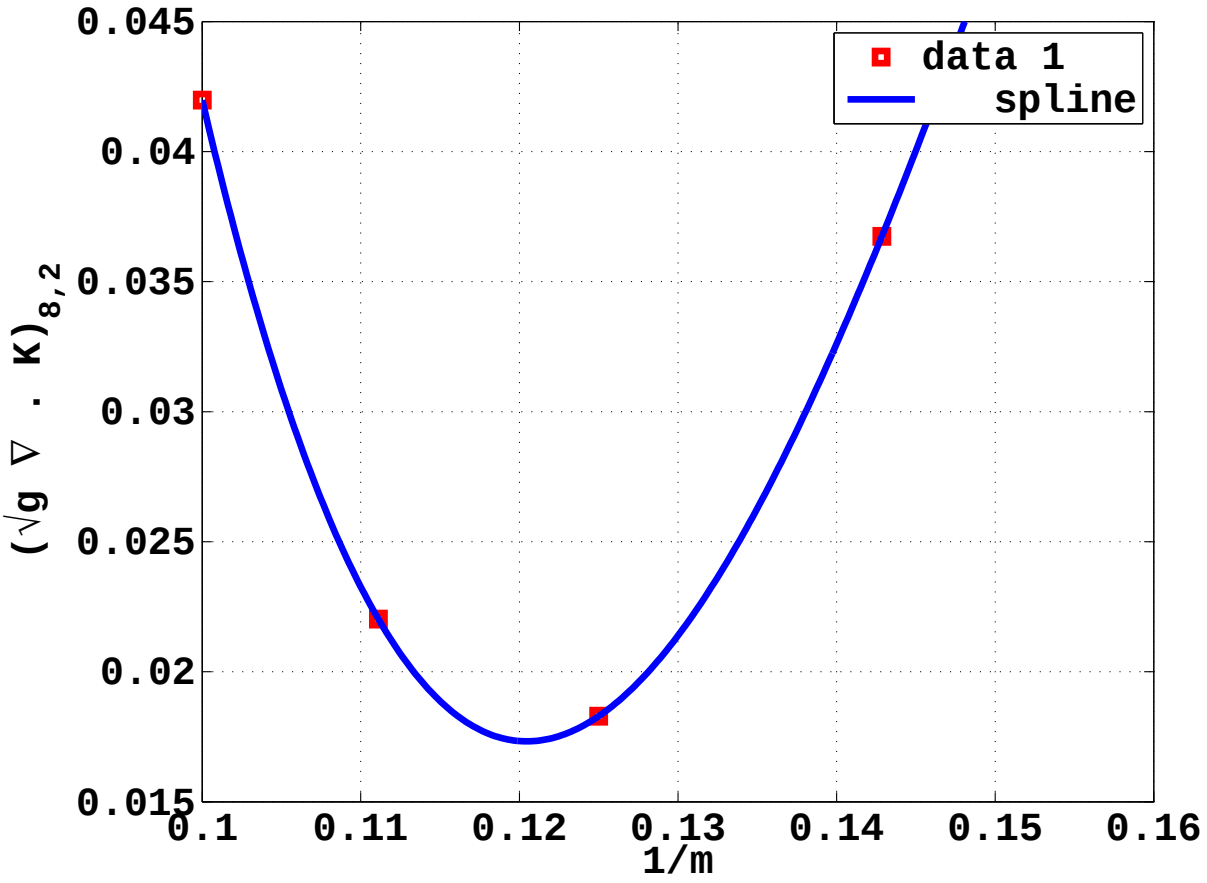

Figure 9: Convergence of the $m_B = 8$, $n_B = 2$ Fourier component of $\sqrt{g}(\boldsymbol{\nabla} \cdot \boldsymbol{K})$ in the Boozer coordinate frame as a function of the inverse of the maximum value of the poloidal mode number m used in the equilibrium computation for the case $B_c = 4.9T$; $\left\langle \beta_{\perp}^{h} \right\rangle / \left\langle \beta_{||}^{h} \right\rangle \simeq 3.4$ (HF side hot particle deposition with $p_{\perp} > p_{||}$) in a 2-period quasiaxisymmetric stellarator. The ordinate has not been normalised so its units are A/m.

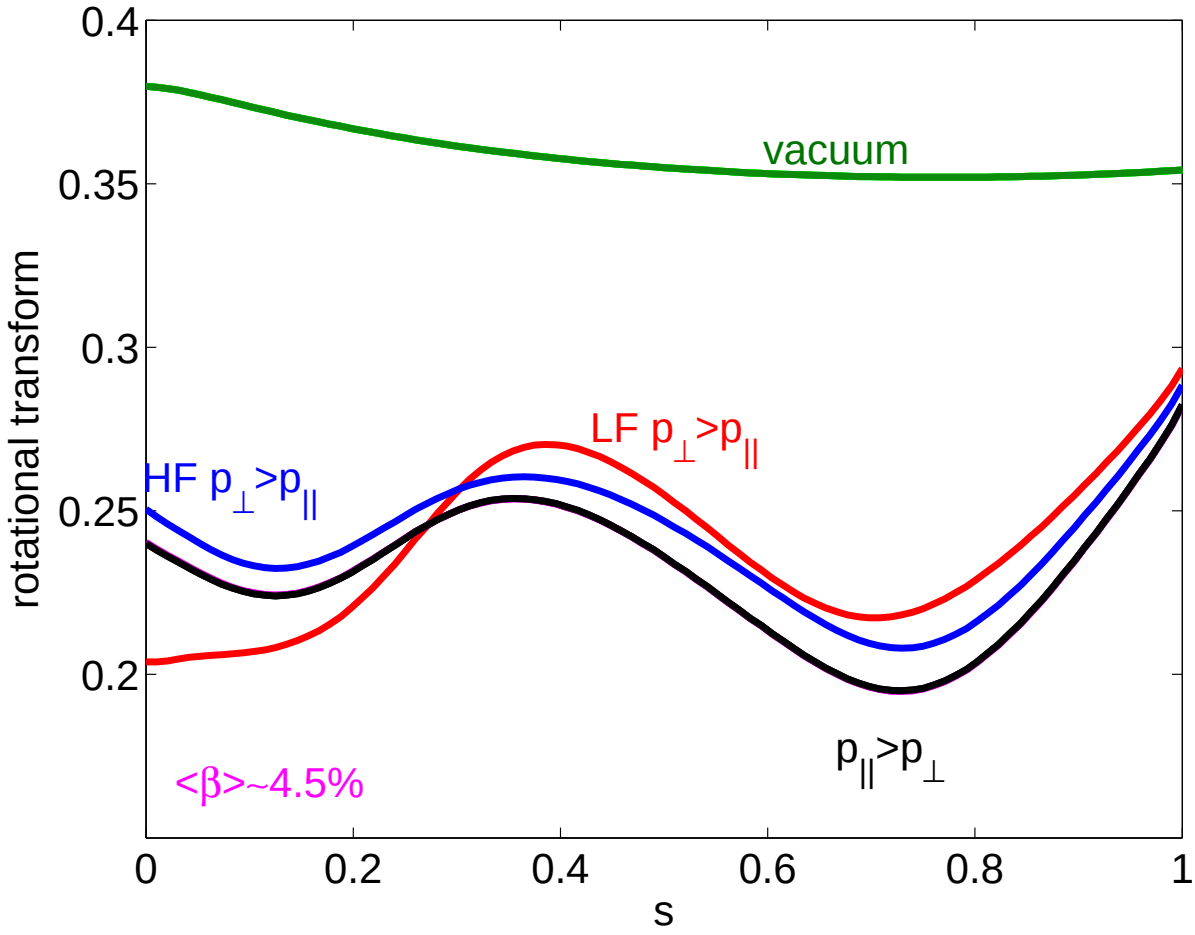

Figure 10: The vacuum (green curve) and the finite $\langle\beta\rangle \simeq 4.5\%$ rotational transform profiles in a 2-field period quasiaxisymmetric stellarator system with off-axis energetic particle deposition. The finite β cases investigated have a) $B_c = 4.9T$; $\left\langle\beta_{\perp}^{h}\right\rangle / \left\langle\beta_{||}^{h}\right\rangle \simeq 3.4$ (HF side hot particle deposition with $p_{\perp} > p_{||}$) (blue curve), b) $B_c = 4.2T$; $\left\langle\beta_{\perp}^{h}\right\rangle / \left\langle\beta_{||}^{h}\right\rangle \simeq 3.4$ (LF side hot particle deposition with $p_{\perp} > p_{||}$) (red curve), c) $B_c = 4.9T$; $\left\langle\beta_{\perp}^{h}\right\rangle / \left\langle\beta_{||}^{h}\right\rangle \simeq 1/3.4$ (HF side hot particle deposition with $p_{||} > p_{\perp}$), d) $B_c = 4.2T$; $\left\langle\beta_{\perp}^{h}\right\rangle / \left\langle\beta_{||}^{h}\right\rangle \simeq 1/3.4$ (LF side hot particle deposition with $p_{||} > p_{\perp}$) (black curve). The curves with $p_{||} > p_{\perp}$ lay approximately on top of one another.

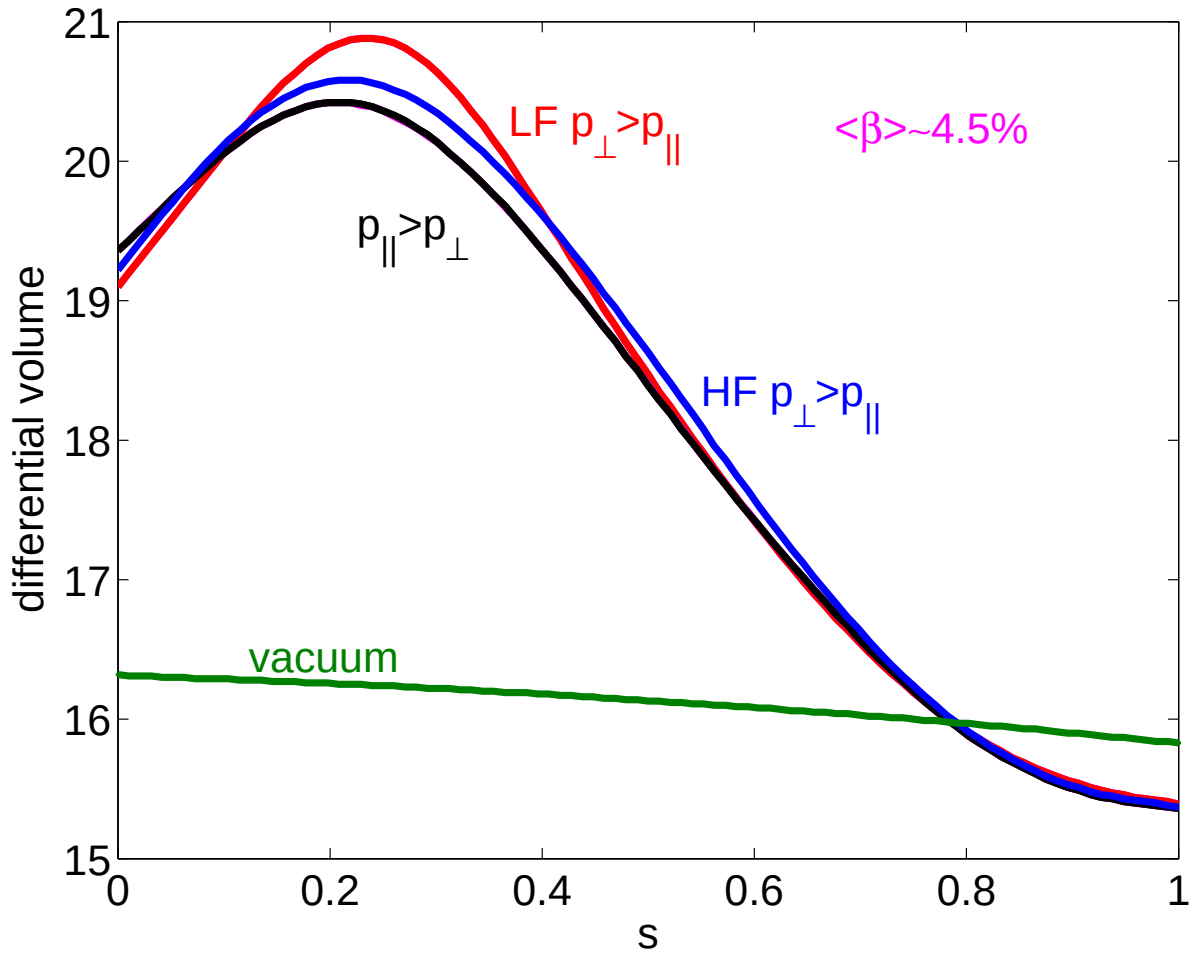

Figure 11: The vacuum (green line) and the finite $\langle\beta\rangle \simeq 4.5\%$ differential volume profiles in a 2-field period quasiaxisymmetric stellarator system with off-axis energetic particle deposition. The finite β cases investigated have a) $B_c = 4.9T$; $\left\langle\beta_\perp^h\right\rangle / \left\langle\beta_{||}^h\right\rangle \simeq 3.4$ (HF side hot particle deposition with $p_\perp > p_{||}$) (blue curve), b) $B_c = 4.2T$; $\left\langle\beta_\perp^h\right\rangle / \left\langle\beta_{||}^h\right\rangle \simeq 3.4$ (LF side hot particle deposition with $p_\perp > p_{||}$) (red curve), c) $B_c = 4.9T$; $\left\langle\beta_\perp^h\right\rangle / \left\langle\beta_{||}^h\right\rangle \simeq 1/3.4$ (HF side hot particle deposition with $p_{||} > p_\perp$), d) $B_c = 4.2T$; $\left\langle\beta_\perp^h\right\rangle / \left\langle\beta_{||}^h\right\rangle \simeq 1/3.4$ (LF side hot particle deposition with $p_{||} > p_\perp$) (black curve). The curves with $p_{||} > p_\perp$ lay approximately on top of one another.

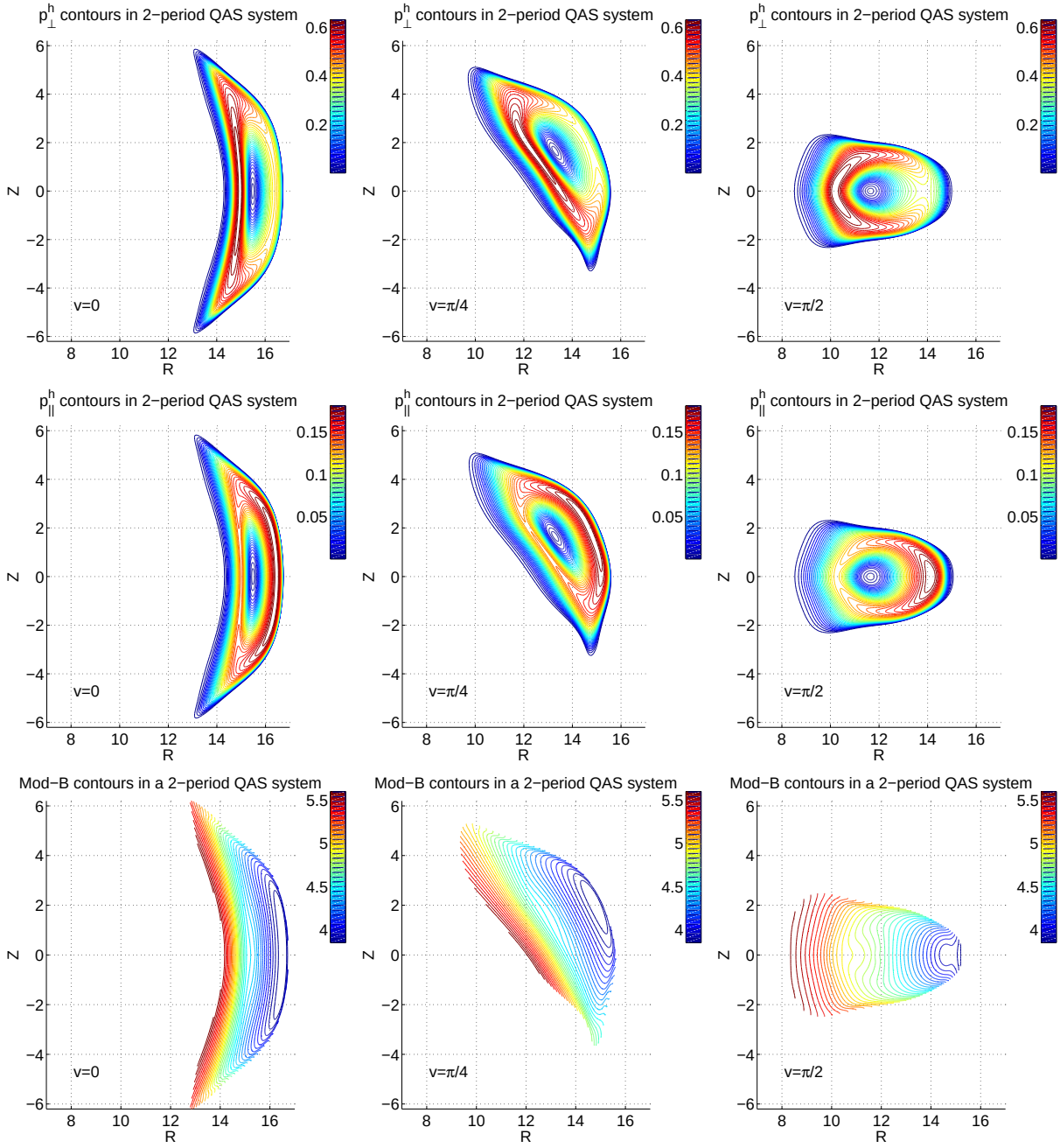

Figure 12: The contours of constant hot particle perpendicular pressure $p_{\perp}^{h}$ (top row), hot particle parallel pressure $p_{||}^{h}$ (middle row) and the mod-B (bottom row) in a 2-field period quasiaxisymmetric stellarator reactor system with high field side energetic particle deposition at $\langle\beta\rangle \simeq 4.5\%$ with large perpendicular anisotropy ($p_{\perp} > p_{||}$) corresponding to $\left\langle\beta_{\perp}^{h}\right\rangle / \left\langle\beta_{||}^{h}\right\rangle \simeq 3.4$ on three cross sections spanning half of a field period.

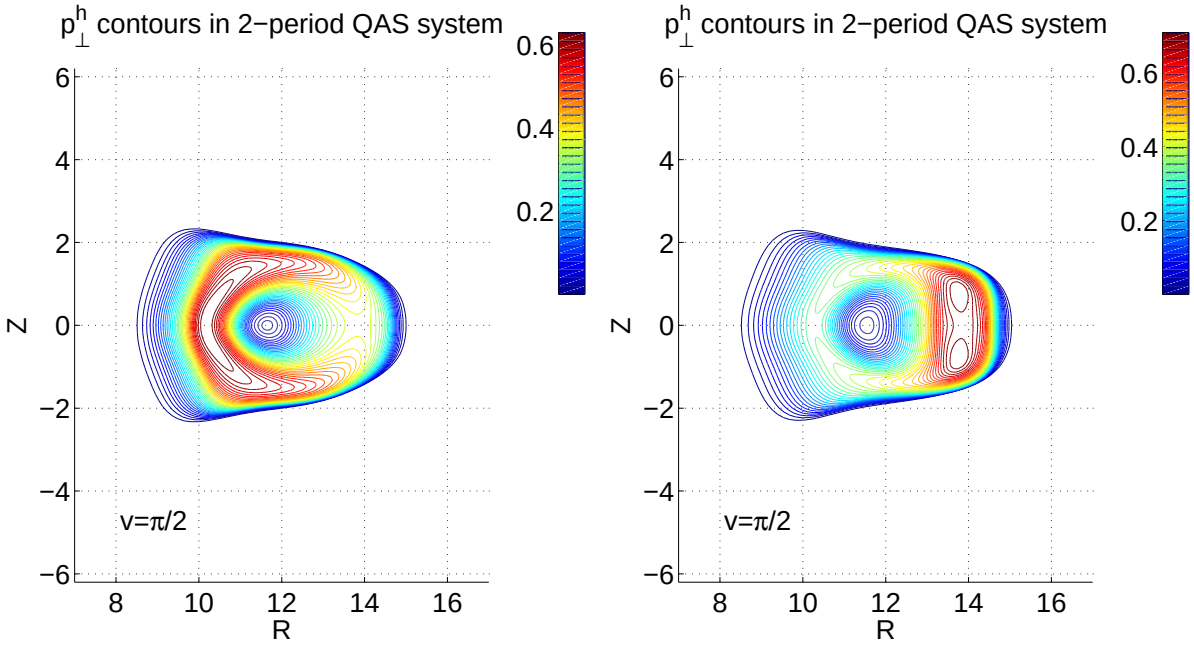

Figure 13: The hot particle perpendicular pressure $p_\perp^h$ contours for $p_\perp > p_{||}$ HF side deposition ($B_C = 4.9T$; $\left\langle \beta_\perp^h \right\rangle / \left\langle \beta_{||}^h \right\rangle \simeq 3.4$) (left) and $p_\perp > p_{||}$ LF side deposition ($B_C = 4.2T$; $\left\langle \beta_\perp^h \right\rangle / \left\langle \beta_{||}^h \right\rangle \simeq 3.4$) (right) at midperiod in a 2-field period quasiaxisymmetric stellarator reactor at $\langle \beta \rangle \simeq 4.5\%$.

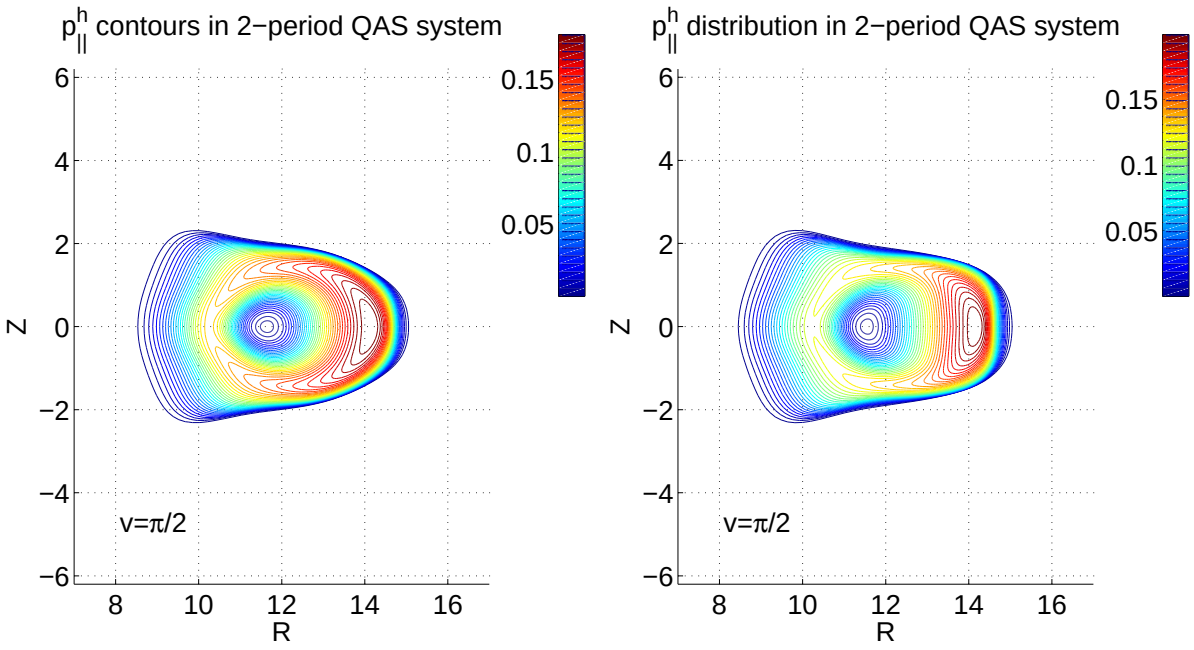

Figure 14: The hot particle parallel pressure $p_{||}^h$ contours for $p_\perp > p_{||}$ HF side deposition ($B_C = 4.9T$; $\left\langle \beta_\perp^h \right\rangle / \left\langle \beta_{||}^h \right\rangle \simeq 3.4$) (left) and $p_\perp > p_{||}$ LF side deposition ($B_C = 4.2T$; $\left\langle \beta_\perp^h \right\rangle / \left\langle \beta_{||}^h \right\rangle \simeq 3.4$) (right) at midperiod in a 2-field period quasiaxisymmetric stellarator reactor at $\langle \beta \rangle \simeq 4.5\%$.

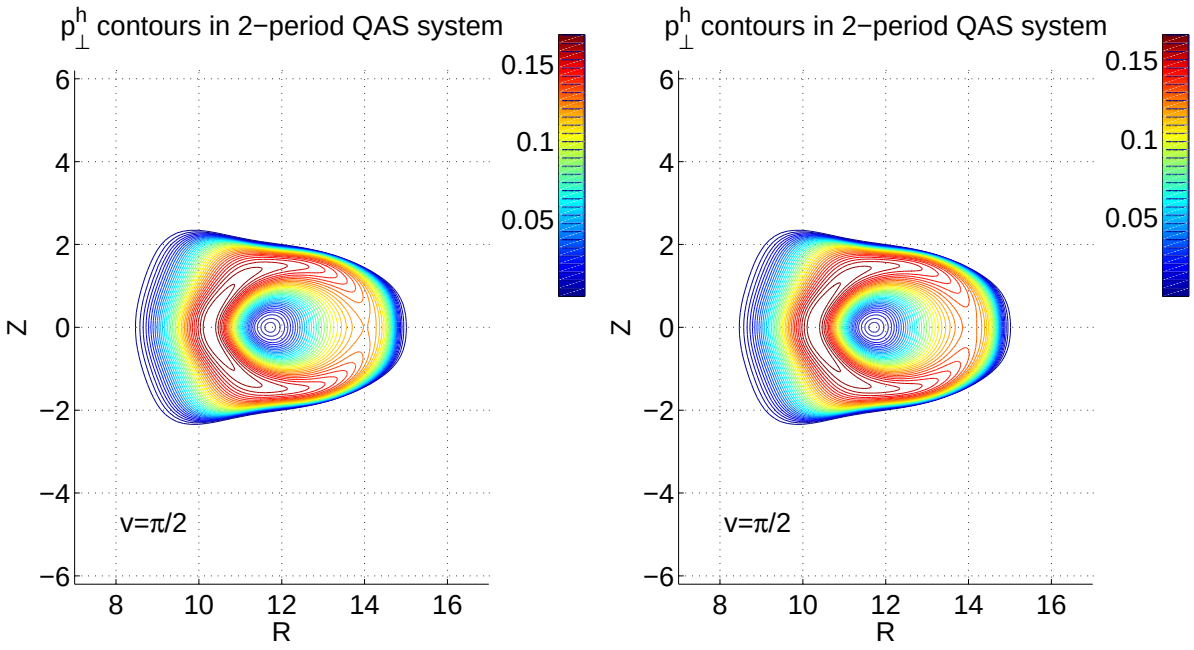

Figure 15: The hot particle perpendicular pressure $p_\perp^h$ contours for $p_{||} > p_\perp$ HF side deposition ($B_C = 4.9T$; $\left\langle \beta_\perp^h \right\rangle / \left\langle \beta_{||}^h \right\rangle \simeq 1/3.4$) (left) and $p_{||} > p_\perp$ LF side deposition ($B_C = 4.2T$; $\left\langle \beta_\perp^h \right\rangle / \left\langle \beta_{||}^h \right\rangle \simeq 1/3.4$) (right) at midperiod in a 2-field period quasiaxisymmetric stellarator reactor at $\langle \beta \rangle \simeq 4.5\%$.

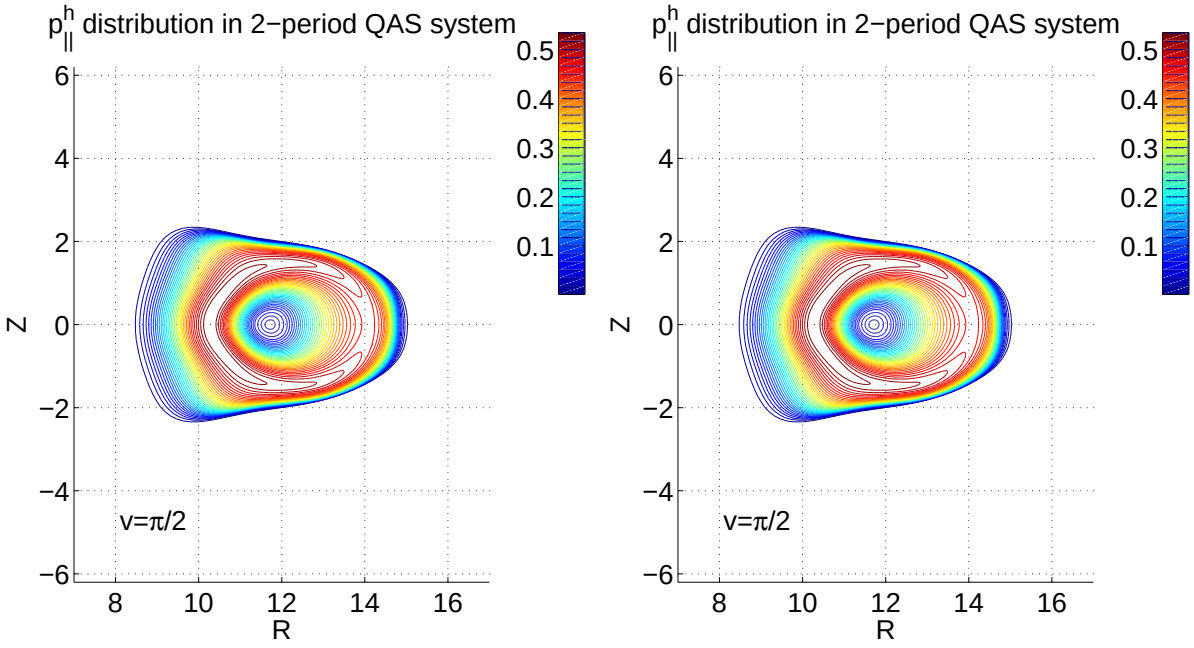

Figure 16: The hot particle parallel pressure $p_{||}^h$ contours for $p_{||} > p_\perp$ HF side deposition ($B_C = 4.9T$; $\left\langle \beta_\perp^h \right\rangle / \left\langle \beta_{||}^h \right\rangle \simeq 1/3.4$) (left) and $p_{||} > p_\perp$ LF side deposition ($B_C = 4.2T$; $\left\langle \beta_\perp^h \right\rangle / \left\langle \beta_{||}^h \right\rangle \simeq 1/3.4$) (right) at midperiod in a 2-field period quasiaxisymmetric stellarator reactor at $\langle \beta \rangle \simeq 4.5\%$.